



- Three-Dimensional Biomass Burning Emission Inventory for
- 2 Southeast and East Asia Based on Multi-Source Data Fusion and
- 3 Machine Learning
- 4 Yinbao Jin^{1,5}, Heng Huang^{2*}, Jian Liu^{3,4}, Yiming Liu⁵, Xiaoyang Chen⁶, Yongqiang, Chen¹, Licheng Li¹,
- 5 Oi Fan^{5,7,8,*}

- 7 Guangzhou Meteorological Satellite Ground Station (Guangdong Meteorological Satellite Remote
- 8 Sensing Center), Guangzhou, 510640, China
- 9 2School of Geomatics, Liaoning Technical University, Fuxin 123000, China
- 10 ³College of Environment and Ecology, Taiyuan University of Technology, Taiyuan 030024, China
- 11 ⁴Shanxi Key Laboratory of Complex Air Pollution Control and Carbon Reduction, Taiyuan University
- 12 of Technology, Taiyuan 030024, China
- 13 School of Atmospheric Sciences, Sun Yat-Sen University, Zhuhai 519082, China
- 14 6Institute of Tropical and Marine Meteorology, China Meteorological Administration, Guangzhou
- 15 510000, China
- 16 Southern Marine Science and Engineering Guangdong Laboratory, Zhuhai 519082, China
- 17 Suangdong Province Key Laboratory for Climate Change and Natural Disaster Studies, School of
- 18 Atmospheric Sciences, Sun Yat-sen University, Guangzhou 510275, China

19

29

- $20 \qquad *\textit{Correspondence to} : Qi \ Fan \ (eesfq@mail.sysu.edu.cn) \ and \ Heng \ Huang \ (huangheng@lntu.edu.cn)$
- 21 Abstract
- 22 Biomass burning (BB) is a major source of atmospheric pollutants in Southeast and East Asia (SEA), yet
- 23 most existing emission inventories lack accurate diurnal cycles and vertical injection profiles, limiting
- 24 the accuracy of air quality and climate simulations. This study develops the Southeast and East Asia Fire
- 25 (SEAF) inventory, an hourly 3 km three-dimensional (3D) emission dataset for 2023, by fusing fire
- 26 radiative power (FRP) from Himawari-8/9 AHI and VIIRS through cloud correction, cross-calibration,
- 27 and a region-vegetation-specific Gaussian diurnal reconstruction with dynamic gap filling. Vertical
- 28 profiles are further constrained using a random forest (RF) Shapley Additive Explanations (SHAP)

framework trained with Multi-angle Imaging SpectroRadiometer (MISR) smoke plume heights (SPH)

- 30 and ERA5 meteorology. The SEAF inventory exhibited strong consistency with TROPOMI CO, showing
- 31 a correlation of R = 0.97 in monthly columns and differing by only 7.81% during a representative event
- 32 on 9 March 2023. Annual PM_{2.5} emissions in SEAF are approximately 2362 Gg y⁻¹, which is 67% lower
- 33 than the Fire INventory from NCAR (FINN) but aligns well with the Fire Energetics and Emissions





- 34 Research (FEER) and the Quick Fire Emissions Dataset (QFED) estimates. The RF-SHAP framework
- 35 successfully predicted SPH, with over 90% of estimates within ± 500 m. This approach corrects the near-
- 36 surface overweighting of conventional schemes by reducing emissions below 0.3 km and enhancing
- 37 injection between 2.7-5.5 km during the spring burning peak, yielding vertical profiles that closely align
- with satellite observations. SHAP analysis identified temperature- and radiation-related factors, 38
- 39 particularly the vertical integral of temperature (Vit) and terrain elevation, as the primary drivers of SPH,
- with additional contributions from FRP, planetary boundary layer height, and seasonal-meteorological 40
- 41 interactions. These advances in both diurnal timing and vertical injection are anticipated to provide an
- 42 observation-driven, hourly 3D BB emission dataset for SEA that can improve the reliability of air quality,
- 43 climate, and policy assessment models.

1. Introduction

44

60

68

- 45 Open biomass burning (BB) exerts substantial impacts on climate, ecosystems, economies, and public
- 46 health by releasing large quantities of aerosols and trace gases into the atmosphere (Pullabhotla et al.,
- 47 2023; Reining et al., 2025; Yu et al., 2022). Black carbon (BC) and primary organic aerosols (POA)
- 48 account for approximately 40-59% and 60-85% of BB aerosol emissions, respectively, while non-
- 49 methane organic gases and greenhouse gases such as methane (CH₄), carbon dioxide (CO₂), and nitrous
- 50 oxide (N2O) contribute significantly to atmospheric chemistry and radiative forcing (Gkatzelis et al.,
- 51 2024). Through direct and indirect effects, these emissions perturb the Earth's radiative balance, alter
- aerosol composition, and modulate cloud and precipitation processes (Crutzen et al., 1979). Under global 52
- 53 warming, wildfire frequency and intensity have increased (Brown et al., 2023; Reining et al., 2025).
- 54 Therefore, accurate quantification of these emissions is essential for evaluating their effects on air quality,
- 55 climate systems, guiding targeted mitigation, and improving carbon inventories (Liu and Popescu, 2022).
- 56 Although total BB emissions in Southeast and East Asia (SEA) are lower than in southern Africa, the
- 57 largest global source region, the regional impacts on cloud properties and radiation remain substantial
- 58 and environmentally consequential (Ding et al., 2021). Most BB inventories in SEA are based on daily
- 59 or monthly FRP products from polar-orbiting sensors such as the Moderate Resolution Imaging

Spectroradiometer (MODIS) and Visible Infrared Imaging Radiometer Suite (VIIRS), which miss

- 61 pronounced diurnal cycles and nocturnal burning. These limitations bias emission estimates in regions
- 62 with frequent cloud cover and small-scale fires (Andela et al., 2015; Liu et al., 2024b, a). Multi-source
- 63 data fusion of geostationary and polar-orbiting FRP based on a top-down approach has emerged as an
- 64 effective way to address these gaps (Li et al., 2022; Nguyen et al., 2023). This multi-source data fusion
- 65 addresses the shortcomings of single data sources, providing a more accurate representation of BB
- 66 emissions. It is particularly beneficial for regions with frequent fires or complex meteorological
- 67 conditions, offering high-resolution data to support regional air quality simulations and significantly
- 2019). For the contiguous United States, Li et al., (2022) integrated Geostationary Operational 69

enhancing the ability to dynamically respond to variations in fire intensity and distribution (Li et al.,

- 70 Environmental Satellite - R Series (GOES-R) and VIIRS produced an hourly 3 km inventory that better
- 71 captured seasonal and diurnal patterns when evaluated against carbon monoxide and fine particulate
- 72 matter from multiple inventories In East Asia, combinations of MODIS, VIIRS, and Himawari have
- 73 yielded hourly products at kilometer scale that improve spatiotemporal characterization (Xu et al., 2023,
- 74 and Xu et al., 2022). However, compared to other inventories, these integrated inventories still exhibit
- 75 significant uncertainties in annual emissions (2-7 times) and monthly emissions (1-48 times) (Xu et al.,

90

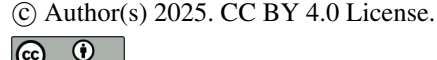
91

104

105

110





77 reconstruct the diurnal cycle of fire emissions, which tends to understate peak burning when observations 78 are missing because of clouds or sampling gaps and may overfill periods with little activity (Li et al., 79 2019). Importantly, our previous work showed that the large spread among available inventories over 80 Southeast Asia strongly influences simulations of aerosol optical properties and radiative forcing (Jin et 81 al., 2024). These results underscore the need for improved inventories with higher spatiotemporal fidelity. 82 Accurate representation of smoke vertical injection is equally critical. Smoke plume height (SPH) 83 determines the vertical distribution of pollutants, affecting transport, removal, and radiative effects (Jin 84 et al., 2024; Li et al., 2023). Although a few models have attempted to account for SPH, they usually rely 85 on fire size and heat flux estimation, which suffers from high computational cost and bias (Driscoll et al., 86 2024). Additionally, inventories such as Integrated System for Fire Information Retrieval and Evaluation 87 (IS4FIRE) estimate SPH using semi-empirical formulas, but their accuracy is limited due to inadequate 88 consideration of meteorological variables (Driscoll et al., 2024; Freitas et al., 2007; Sofiev et al., 2012). 89 To address these challenges, researchers have gradually introduced machine learning methods to capture

the nonlinear relationships between meteorological factors and BB characteristics (Brown et al., 2023;

Wang and Wang, 2020). However, there is still a relative lack of quantitative studies on the relationship

2023b; Zhang et al., 2014). In addition, most inventories apply a climatological Gaussian scheme to

92 between SPH and meteorological factors. In-depth exploration of the driving mechanism of plume rises 93 and its integration into the three-dimensional (3D) BB emission inventory is important for improving the 94 accuracy of the emission inventory as well as the ability of global/regional atmospheric modeling. 95 This study develops the Southeast and East Asia Fire (SEAF) emission inventory, an hourly 3-km 96 resolution BB emission product covering SEA in 2023. SEAF was generated by fusing FRP data from 97 Advanced Himawari-9 Imager (AHI), VIIRS, and NOAA's Joint Polar Satellite System (NOAA20), with 98 dynamic adjustment of Gaussian-fitted FRP daily cycles to improve temporal accuracy. The inventory 99 was validated against Tropospheric Monitoring Instrument (TROPOMI) observations and five 100 commonly used BB emission inventories. A 3D version is further constructed by combining Multi-angle 101 Imaging Spectroradiometer (MISR) plume heights with ECMWF Reanalysis v5 (ERA5) meteorology 102 through a machine-learning framework. The resulting products will provide improved data support for 103 regional air-quality and climate modeling applications.

2. Data and Methodology

2.1 Satellite data

To characterize BB emissions across SEA, four representative subregions were delineated using landcover and climate classifications as shown in Figure 1. This spatial framework supports the integration of geostationary and polar-orbiting satellite observations, laying the foundation for subsequent FRPbased emission inventory development.

2.1.1 Satellite-based Fire Radiative Power

Satellite observations provide critical information on FRP, which serves as BB emission estimates. In this study, we mainly use two FRP products derived from polar-orbiting and geostationary satellites. The 375m I band Level 2 active fire product from the VIIRS sensor provides observations from NASA/NOAA's Suomi National Polar-orbiting Partnership (S-NPP) and NOAA-20 satellites (Schroeder et al., 2024). The VIIRS sensor was first deployed on the Suomi NPP satellite in October 2011 and has





- since been extended with support for NOAA-20 and NOAA-21 satellites (Giglio et al., 2016). The first
- 117 fire hotspot detection from the VIIRS sensor occurred on January 19, 2012. The 375 m data supplements
- the MODIS fire detection. Both MODIS and VIIRS products show good consistency in hotspot detection,
- 119 but the VIIRS 375 m product improves spatial resolution, offering better response for relatively smaller
- 120 fire areas and providing improved large fire perimeter mapping(Schroeder et al., 2014). The 375m data
- 121 product also improves nighttime performance, making these data ideal for use in support of fire
- 122 management (e.g., near-real-time alarm systems) and other scientific applications that require improved
- fire mapping fidelity (Csiszar et al., 2014).
- 124 The FRP data provided by the Himawari-8/9 satellite comes from its Advanced Himawari Imager (AHI)
- 125 sensor, which has a spatial resolution of 2 km and a temporal resolution of 10 minutes, offering full disk
- coverage (60°N-60°S, 80°E-160°W) (Bessho et al., 2016). The FRP is determined using a dual-spectral
- method applied to data from the 2.3 µm and 3.9 µm bands (JAXA/EORC, 2020). Since October 2015, the
- Himawari satellite has consistently supported fire monitoring and disaster response with its high-
- 129 precision imaging capabilities. Himawari-8 has moderate spatial resolution, very high temporal
- 130 resolution, and a fixed observation area, making it particularly suitable for real-time monitoring of
- wildfires in SEA (Xu et al., 2022). Furthermore, unlike MODIS or Fengyun-3D fire products, which fail
- to capture nighttime events, Himawari-8 has the advantage of continuously monitoring wildfires after
- sunset, making it a valuable tool for replacing manual inspections of nighttime wildfires (Chen et al.,
- 2023). Himawari-8 is highly resistant to smoke and thin clouds, and it is very sensitive to small fires,
- providing valuable real-time fire information for wildfire management (Xu and Zhong, 2017). However,
- existing Himawari-8 fire products show poor consistency with MODIS data (Jang et al., 2019). Therefore,
- we first correct the Himawari-8/9 fire products using the methodology of Li et al., (2022) before
- 138 performing data fusion.

2.1.2 TROPOMI CO

- 140 The Tropospheric Monitoring Instrument (TROPOMI) aboard the Sentinel-5 (S5-P) satellite measures
- 141 the total column concentration of CO, providing daily global coverage with a high spatial resolution of
- 142 5.5×7 km² (Landgraf et al., 2018). The instrument was launched on October 13, 2017 and can measure
- within the visible (270-500 nm), near-infrared (675-775 nm), and short-wave infrared (SWIR, 2305-2385
- 144 nm) ranges (Borsdorff et al., 2023). The TROPOMI CO data clearly shows strong sources such as
- wildfires, with a small mean difference $(3.2 \pm 5.5\%)$ and a high correlation (R=0.97) between TROPOMI
- and CAMS (Borsdorff et al., 2018). Li et al., (2022) and Griffin et al., (2024) have validated TROPOMI
- 147 CO as a reliable dataset for assessing the CO reliability of inverted BB emissions. In this paper, we also
- used these data and Eq. (1) to evaluate our fused inverted CO data for BB emissions.

$$M'_{co} = \sum_{i=1}^{n} \left(\rho_{sm}^{i} - \rho_{bg} \right) \times A^{i} \times M \tag{1}$$

- 149 M'_{co} represents the total CO emissions for a given fire sample. ρ^i_{sm} and A^i are the observed total column
- 150 CO concentration (mol m⁻²) and the pixel area (m²) for the i smoke pixel. ρ_{bg} is the mean column density
- of background pixels. M is the molecular mass of CO ($M = 28.01 \text{ g mol}^{-1}$).

166

181

182

183

184 185

186

187

188

189

190

191

192





2.1.3 MISR plume height dataset

153 SPH observations were obtained from the MISR Plume Height Project II, which assembled a dataset of 154 smoke plumes for the summers of 2008 to 2011 and for 2017 and 2018 (Nastan et al., 2022). The MISR 155 instrument onboard Terra acquires imagery at nine viewing angles, and heights are retrieved by stereo parallax using the MISR Interactive Explorer (MINX). Because digitization in MINX is labor intensive, 156 157 data collection was conducted over multiple years by teams at the Jet Propulsion Laboratory and the 158 Goddard Space Flight Center together with student groups at the University of Sheffield (Val Martin et al., 2018). Under favorable conditions the vertical accuracy can reach approximately 200 m (Nelson et 159 160 al., 2013). The MISR smoke plume records have been widely used to characterize wildfire injection heights and have become an important observational constraint in regional and global studies (Ke et al., 161 162 2021; Zhu et al., 2018). For this study the MISR Enhanced Research and Lookup Interface (MERLIN) 163 was used to extract 2127 plume height samples from Southeast and East Asia during 2017 and 2018 as 164 shown in Figure S1. These samples served as training data for the machine learning based estimation of 165 SPH.

2.2 ERA5 and Other Biomass Burning emissions

167 ERA5 is the fifth generation of global climate reanalysis dataset released by the European Center for 168 Medium-Range Weather Forecasts (ECMWF), which is widely used in global climate and weather 169 research. The ERA5 hourly meteorological data used in this study are sourced from the Climate Data 170 Store, offering a spatial resolution of 0.25° × 0.25°. This dataset covers several key meteorological 171 variables relevant to BB (Bell et al., 2021). Variables relevant to BB include 2m temperature, 2m dew 172 point temperature, 10m wind speed components, and precipitation, among others, which jointly provide 173 the meteorological context for fire occurrence and plume development (Dong et al., 2021; Kim et al., 174 2025; Vitolo et al., 2020). ERA5 variables were combined with FRP from VIIRS and Himawari-8/9, 175 together with MISR SPH, to train a machine learning model to predict plume injection height in 2023. 176 The set of ERA5 predictors used is summarized in Table S1. To assess the accuracy of the fused BB 177 emission inventory, a detailed spatiotemporal comparison was performed against major international 178 inventories including the Global Fire Assimilation System (GFAS), the Fire INventory from NCAR 179 (FINN), the Fire Energetics and Emissions Research (FEER), the Quick Fire Emissions Dataset (QFED), 180 and IS4FIRES (Table S2).

2.3 Methodologies

Figure 2 illustrates the framework for estimating hourly 3D BB emissions. Active fire observations from Himawari 9 AHI, Suomi NPP VIIRS I band, and NOAA 20 VIIRS I band are gridded at 3 km, corrected for cloud effects, and fused. Historical AHI records from 2016 to 2023 were analyzed to derive statistics on burn duration and observational gaps, which were then applied with Gaussian fitting to construct hourly FRP diurnal cycles. During intense burning periods, the diurnal curves were dynamically adjusted to recover missing peaks while preventing overestimation. Two products were generated: a 2D inventory providing surface emissions, and a 3D inventory that incorporates vertical injection by applying a RF model using FRP, ERA5 meteorology, and MISR SPH to predict injection height and allocate emissions vertically. This fused product is referred to as the Southeast and East Asia Fire (SEAF) inventory. This study focuses on 2023, a year that offered a unique convergence of consistent observations from the newly operational Himawari-9 and a scientifically significant, intense fire season driven by El Niño,

198

199

200

201

202

203

204

205

206





- 193 ideal for validating the framework (Jong, 2024). Finally, the 2D SEAF inventory was evaluated against
- 194 TROPOMI CO and six major global emission inventories, while the 3D SEAF inventory was assessed
- 195 using MISR, Cloud-Aerosol Lidar and Infrared Pathfinder Satellite Observations (CALIPSO),
- 196 IS4FIRES, and GFAS data.

2.3.1 Data calibration

To facilitate subsequent air-quality modeling applications, all datasets were regridded to a spatial resolution of $0.03^{\circ} \times 0.03^{\circ}$. During aggregation, the FRP within each grid cell was summed, while the geolocation of individual fire detections was retained to represent the combined intensity of co-occurring events. This procedure is consistent with the native generation of the VIIRS I band FRP product and aligns with the objectives of emission inventory construction. For cloud correction, the cloud fraction in each grid cell at the satellite overpass time was computed using the VIIRS-I SDR terrain-corrected geolocation (GITCO) files. Cloud fraction was defined as the ratio of cloud pixels to the total number of pixels in the cell, with cloud pixels identified from their latitude and longitude coordinates. The resulting calibration was then applied to the polar-orbiting observations as specified in Eq. (2).

$$FRP^{V} = \begin{cases} \frac{FRP^{V}_{aggregation}}{1 - \beta + \alpha \times \beta^{2}} & \beta \le 95\% \\ FRP^{V}_{aggregation} & \beta > 95\% \end{cases}$$
 (2)

- where $FRP_{aggregation}^{V}$ represents the aggregated FRP values at the grid points after regridding the
- VIIRS data. FRP^V is the cloud-corrected FRP value. β is the cloud fraction, and when the cloud fraction
- 209 exceeds 95%, cloud correction is not applied to avoid overestimation. α is the secondary coefficient,
- which is set to 0.25 according to the testing described in Li et al., (2022).

2.3.2 Geostationary satellite FRP calibration

- 212 Given the relatively large zenith angle of the Himawari-8/9 satellite over Northeast China (Region 4,
- Figure 1), it is essential to apply appropriate calibration to the FRP data. In this study, cloud-corrected
- 214 polar-orbiting satellite data are used as the calibration reference for the Himawari satellite at matching
- 215 times and location. The calibration formula is given by Eq. (3).

$$\overline{FRP_i^{AHI}} = FRP_i^{AHI} \times (1 + r_i) \tag{3}$$

- where FRP_i^{AHI} and $\overline{FRP_i^{AHI}}$ represent the FRP of fire pixel i before and after calibration, respectively,
- and r_i is the calibration factor. The calibration factor is calculated based on common point pairs, which
- 218 are obtained by matching AHI and VIIRS observations. Specifically, common point pairs are defined
- 219 here as grid points at the same location that are simultaneously detected as fire points in both the
- 220 geostationary and polar-orbiting fire product. "Simultaneously" indicates that the observation times differ
- by no more than ± 5 minutes. If there are multiple VIIRS detections within ± 5 minutes that match an AHI
- 222 fire point, the point with the smallest time difference is selected for matching. For the i common point
- pair, the calibration factor is given by Eq. (4).





$$r_i = \frac{FRP_i^{VIIRS} - FRP_i^{AHI}}{FRP_i^{AHI}} \tag{4}$$

- Where FRP_i^{VIIRS} and FRP_i^{AHI} are the fire radiated power of the VIIRS and AHI of the corresponding
- point pair, respectively.
- 226 In addition, when no common point pair is available, a dynamic calibration factor and an alternative
- 227 calibration factor are established, depending on whether common point pairs exist at other times of the
- day for that fire pixel. Among these, the dynamic calibration factor is defined in Eq. (5)

$$r_{d,j} = \frac{1}{n_d} \sum_{i=1}^{n_d} r_i \tag{5}$$

- Where $r_{d,j}$ is the dynamic calibration factor for pixel j on day d, and n_d is the number of common
- point pairs for that pixel on day d across different time instances.
- 231 For fire points captured by the geostationary satellite, a significant fraction lack corresponding common
- 232 point pairs in the polar-orbiting satellite record on the same day. To address this, an alternative calibration
- 233 factor is introduced. Previous studies have shown that BB fuel characteristics are similar within the same
- land cover type, and that monthly climate conditions are also comparable in SEA (Huang et al., 2024;
- 235 Yin, 2020). Therefore, the calibration factor is calculated for each month and vegetation type based on
- the available common point pairs and then averaged, as represented by Eq. (6).

$$r_{m,l} = \frac{1}{n_{m,l}} \sum_{j=1}^{n_{m,l}} r_j \tag{6}$$

- Where $r_{m,l}$ is the alternative calibration factor for month m and land cover type l, and $n_{m,l}$ is the
- 238 number of common point pairs for month m and land cover type l. The results of the alternative
- 239 calibration factors are shown in Table S3.
- 240 Previous studies have shown that calibrated geostationary and polar-orbiting satellite data exhibit
- 241 improved consistency, and that fusion of these datasets can compensate for limitations in the spatial and
- temporal resolution of individual datasets (Li et al., 2022; Zhang et al., 2012). For air quality modeling
- 243 applications, the temporal resolution of the fusion was set to 1 hour, which satisfies the need for high
- 244 temporal detail while avoiding potential incompatibility from excessively high resolution (López-Noreña
- et al., 2022). Specifically, the results were averaged within 1-hour intervals, while the spatial resolution
- was retained at 0.03°. Given the relatively high quality of polar-orbiting satellite data, these observations
- 247 were prioritized in the fusion process, while geostationary satellite data were used to supplement missing
- 248 detections. The specific fusion method is set in Eq. (7).





$$FRP_i^{fuse} = \begin{cases} FRP_i^{VIIRS} & VIIRS FRP > 0\\ \overline{FRP_i^{AHI}} & VIIRS FRP < 0 \text{ and } AHI FRP > 0\\ 0 & VIIRS FRP < 0 \text{ and } AHI FRP < 0 \end{cases}$$
(7)

Where FRP_i^{fuse} represents the fused fire radiative power for pixel i, FRP_i^{VIIRS} represents the FRP for

pixel i as detected by VIIRS, $\overline{FRP_i^{AHI}}$ represents the fire radiative power for pixel i after calibration

251 by AHI.

252

267

268

269

270

271

272

273

2.3.3 FRP diurnal cycle

The AHI FRP diurnal climatology was developed to fill missing observations caused by cloud cover, 253 254 smoke, and sensor detection limits (Li et al., 2019). Prior to reconstruction, fire duration statistics were 255 derived for four climatic regions and five vegetation types using Himawari-8/9 records from 2016 to 256 2023. Figure S2 shows that most events last 1-2 hours, and the probability of durations exceeding 3 257 hours ranges from 11% to 31%. Therefore, in reconstructing the FRP diurnal cycle, not all fire events 258 were extended across multiple time periods. Figure 3 characterizes periods of sustained burning of at 259 least 3 hours, showing that high burning windows vary across regions and vegetation types. For example, 260 cropland in Region 1 peaks between 01-03 UTC, whereas other regions peak between 06-13 UTC. The 261 frequency of sustained burning (≥ 0.9) also varies, reflecting distinct fire activity regimes. These 262 differences were explicitly accounted for in reconstructing the diurnal cycle. Table 1 reports the 263 maximum duration of continuous high-intensity burning (T_gap) and the corresponding high burning 264 windows used for filling. When two high burning windows occur, they are merged and treated as continuous burning if the time gap is shorter than max(T_gap1, T_gap2) and if the mean frequency within 265 266 the gap is at least 0.5.

the gap is at least 0.5.

After performing the high burning period statistics, curve fitting of the FRP climatological daily cycle is required to fill the missing FRP data. Figure S3 shows that the AHI FRP climatological diurnal cycle for each region consistently follows a unimodal Gaussian curve. Previous studies have indicated that because the FRP diurnal cycle follows a unimodal bell-shaped curve, Gaussian function fitting can be used to reconstruct the FRP climatological diurnal cycle (Vermote et al., 2009; Xu et al., 2022). In this paper, the Gaussian function is improved by adding a vertical adjustment factor (d) to adjust the curve to the FRP distribution of a specific fire event with the following Eq. (8).

$$FRP(t) = ae^{\frac{-(t-b)^2}{2c^2}} + d ag{8}$$

274 Where a, b, c are variable parameters that adjust the vertical scaling of the curve, the peak position and 275 the width of the curve, respectively, which are mainly related to the land class. The parameters a, b, c, d 276 were dynamically adjusted using the least squares method if the number of satellite captures on the day 277 of a specific fire event was able to reconstruct the daily cycle based on the Gaussian function (≥ 4 times), 278 while d was dynamically adjusted based on the day's data only if the number of satellite captures was 279 insufficient to reconstruct the daily cycle or if the reconstruction of the daily cycle was not good enough 280 $(r^2<0.8)$, whereas a, b, c were fixed values calculated based on the historical data in ecological regions 281 and land classes.





282 2.3.4 Construction of emission inventories

- 283 The hourly FRP product, after fusion and filling, is further used to construct the Fire Radiative Energy
- 284 (FRE) using the following Eq. (9).

$$FRE_{h,(i,j)} = \int_{t_1}^{t_2} FRP_r dt \tag{9}$$

- Where $FRE_{n,(i,j)}$ (MJ) represents the FRE produced by the fire point (i,j) from time t_1 to t_2 , FRP_r
- is the reconstructed hourly FRP.
- 287 Dry Matter (DM) refers to the weight of the material in BB that does not include water content. The
- consumption of DM is proportional to the generated flame heat (Koster et al., 2015). Based on the value
- 289 of FRE, the DM consumed during BB over a given period can be estimated, as shown in Eq. (10).

$$DM_{h,(i,j)} = FRE_{h,(i,j)} \times F_{BC} \tag{10}$$

- Where $DM_{h,(i,j)}$ (kg) represents the DM consumed by the fire point (i,j) during one hour of
- combustion, which is proportional to the FRE generated. F_{BC} is the biomass combustion factor. previous
- 292 studies have shown that the relationship between DM mass of manzanita and FRE can be expressed as a
- slope of 0.368 ± 0.015 kg MJ⁻¹ (Wooster et al., 2005), for every 1 MJ of FRE emitted, about 0.368 ± 0.015 kg MJ⁻¹ (Wooster et al., 2005), for every 1 MJ of FRE emitted, about 0.368 ± 0.015 kg MJ⁻¹ (Wooster et al., 2005), for every 1 MJ of FRE emitted, about 0.368 ± 0.015 kg MJ⁻¹ (Wooster et al., 2005), for every 1 MJ of FRE emitted, about 0.368 ± 0.015 kg MJ⁻¹ (Wooster et al., 2005), for every 1 MJ of FRE emitted, about 0.368 ± 0.015 kg MJ⁻¹ (Wooster et al., 2005), for every 1 MJ of FRE emitted, about 0.368 ± 0.015 kg MJ⁻¹ (Wooster et al., 2005), for every 1 MJ of FRE emitted, about 0.368 ± 0.015 kg MJ⁻¹ (Wooster et al., 2005), for every 1 MJ of FRE emitted, about 0.368 ± 0.015 kg MJ⁻¹ (Wooster et al., 2005), for every 1 MJ of FRE emitted, about 0.368 ± 0.015 kg MJ⁻¹ (Wooster et al., 2005), for every 1 MJ of FRE emitted, about 0.368 ± 0.015 kg MJ⁻¹ (Wooster et al., 2005), for every 1 MJ of FRE emitted, about 0.368 ± 0.015 kg MJ⁻¹ (Wooster et al., 2005), for every 1 MJ of FRE emitted, about 0.368 ± 0.015 kg MJ⁻¹ (Wooster et al., 2005), for every 1 MJ of FRE emitted, about 0.368 ± 0.015 kg MJ⁻¹ (Wooster et al., 2005), for every 1 MJ of FRE emitted, about 0.368 ± 0.015 kg MJ⁻¹ (Wooster et al., 2005), for every 1 MJ of FRE emitted, about 0.368 ± 0.015 kg MJ⁻¹ (Wooster et al., 2005), for every 1 MJ of FRE emitted, about 0.368 ± 0.015 kg MJ⁻¹ (Wooster et al., 2005), for every 1 MJ of FRE emitted, about 0.368 ± 0.015 kg MJ⁻¹ (Wooster et al., 2005), for every 1 MJ of FRE emitted, about 0.368 ± 0.015 kg MJ⁻¹ (Wooster et al., 2005), for every 1 MJ of FRE emitted, about 0.368 ± 0.015 kg MJ⁻¹ (Wooster et al., 2005), for every 1 MJ of FRE emitted, about 0.368 ± 0.015 kg MJ⁻¹ (Wooster et al., 2005), for every 1 MJ of FRE emitted, about 0.368 ± 0.015 kg MJ⁻¹ (Wooster et al., 2005), for every 1 MJ of FRE emitted, about 0.015 ± 0.015 kg MJ⁻¹ (Wooster et al., 2005), for every 1 MJ of FRE emitted, about 0.015 ± 0.015 kg MJ⁻¹ (Wooster
- 294 0.015 kg of manzanita DM is consumed. On the other hand, Freeborn et al., (2008) proposed a more
- widely applicable BB coefficient of about 0.453 ± 0.068 kg MJ⁻¹ through an experimental study of
- different plant fuel types. Therefore, this paper chose to adopt 0.453 ± 0.068 kg MJ⁻¹ as the biomass
- 297 combustion coefficient to estimate the amount of DM consumed for one hour of combustion at the fire
- 298 point.
- 299 The various emissions generated by biomass combustion can be estimated using the DM consumption
- and the corresponding emission factor (EF). The emission calculation formula is as shown in Eq. (11).

$$E_x = DM_{h,(i,j)} \times EF_x \tag{11}$$

- Where $E_x(kg)$ represents the emission of substance x (such as CO₂, CO, NO_x, etc.) from the fire
- 302 point(i,j) in one hour, EF_x (g kg⁻¹) is the corresponding EF for each substance, which characterizes
- 303 the amount of a specific chemical produced per kilogram of DM burned. Andreae, (2019) conducted a
- 304 comprehensive analysis and compilation of numerous research results. This study selects representative
- 305 emission categories for BB emission estimation. The selected BB EFs for different regions are shown in
- 306 Table 2.

307

2.3.5 Random Forest prediction of SPH and SHAP models

- 308 RF is an ensemble learning method based on the Bagging (Bootstrap Aggregating) principle, proposed
- 309 by Breiman, (2001). Owing to its strong nonlinear modeling capability and scalability, it has been widely
- applied in meteorological and environmental studies to relate atmospheric variables to land surface processes (Üstek et al., 2024; Wang and Wang, 2020). For example, Agrawal et al., (2023) used machine
- 312 learning techniques, along with ERA5 meteorological variables, to build a multivariate regression model





- 313 for wildfire characteristics (such as burned area), successfully predicting the occurrence of large wildfires.
- Moreover, Briggs, (1969) proposed a method for calculating the rise of wildfire plumes based solely on
- buoyancy terms, modeling the heat released by the fire, wind speed, and friction velocity (Haugen, 1982).
- 316 This method is suitable for small-scale wildfires, such as those observed in prescribed burns (Achtemeier
- 317 et al., 2011). However, these methods are limited in their applicability to large-scale wildfires or plume
- 318 rise under complex meteorological conditions (Ferrero et al., 2019). To characterize the relationship
- 319 between wildfire plume rise and meteorological controls, an RF multivariate regression was trained using
- 320 MISR plume heights, ERA5 meteorology, and satellite-derived FRP. The model predicts SPH, which is
- 321 then used to allocate emissions vertically. Following guidance from the Texas Commission on
- 322 Environmental Quality, (2022) and the IS4Fire vertical allocation scheme (Sofiev et al., 2009), 90 % of
- 323 the hourly column emissions are assigned to the upper two-thirds of the predicted plume and 10 % to the
- 324 lower one-third, yielding five vertical layers in total.
- 325 SHAP (Shapley Additive Explanations) is an explanation tool based on game theory, used to quantify the
- 326 contribution of each feature to the predictions of a machine learning model (Mangalathu et al., 2020). By
- 327 calculating the marginal contribution of each feature to the model prediction, SHAP provides
- 328 transparency and interpretability for complex models, such as Random Forest, revealing interactions
- 329 between features (Ekanayake et al., 2022). In this study, in addition to applying the RF model for
- 330 multivariate regression, SHAP was also employed to further analyze the contribution of each
- 331 meteorological variable to SPH.

3. Result

332

333334

335

336

337

338

339

340

341

342

343

344

345

346

347

348 349

350

351

352

353

3.1 VIIRS and AHI Data Correction

Figure 4 illustrates the spatial distribution of gridded FRP data derived from VIIRS and AHI, demonstrating the impact of cloud correction algorithms implemented through Eq. (2)-(7). The uncorrected datasets reveal that elevated FRP values are predominantly concentrated within Region 2 for both sensor systems. Due to its superior temporal resolution (10 min revisit time), AHI consistently records higher FRP magnitudes compared to VIIRS. Chen et al., (2022) demonstrated that Himawari-8, with its 2km spatial resolution, detects significantly more fire events than MODIS and VIIRS, consequently yielding elevated FRP measurements. Furthermore, comparisons of thermal anomaly observations from drones with both VIIRS and Himawari-8 data indicate that VIIRS measurements are more reliable. Therefore, this study employs cloud-corrected VIIRS data as a benchmark for calibrating AHI FRP. Region 1, characterized by tropical rainforest (Af) and tropical monsoon (Am) climates, experiences high temperatures, humidity, and frequent rainfall, resulting in extensive cloud cover and frequently underestimated satellite-derived FRP measurements. Prior to cloud correction, the mean VIIRS FRP values in this region are 11.44 ± 21.07 MW and 11.24 ± 20.65 MW in Figure 4 (a) and (d). Following cloud correction, the mean FRP exhibits an approximate 7% increase. Region 2, defined by Am and tropical wet and dry (Aw) climates, is characterized by intense monsoon activity and frequent fire occurrences. After correction, VIIRS FRP increases by 0.6 MW, demonstrating that cloud correction not only mitigates cloud-induced errors but also enhances fire intensity estimation, enabling more accurate detection of fire activity. Regions 3 and 4 similarly exhibit increased VIIRS FRP values following cloud correction, whereas calibrated AHI FRP generally shows a decreasing trend across the study area. However, in regions with substantial BB emissions, such as northern Laos, AHI FRP still





- 354 increases, likely as cloud correction reveals additional fire activity, thereby yielding higher observed FRP
- 355 values.

357358

359

360361

362

363

364

365

366

367

368

369

370

371

372

373

374

375

376

377

378

379

380

381

382

383

384 385

386 387

388 389

390

391

392

393

394

3.2 Reconstruction of the FRP daily cycle

3.2.1 Gaussian-based fitting of FRP diurnal climatology

To establish a robust foundation for accurately filling temporal gaps in BB emission inventories, climatological diurnal FRP cycles were fitted using Gaussian functions. Historical Himawari-8/9 (AHI) FRP observations from 2016 to 2023 were used to derive climatological diurnal cycles for four representative regions (Regions 1-4) and five vegetation types (cropland, forest, grassland, peatland, and shrubland) in Figure S4. The Gaussian fitting performed well in most regions and vegetation types with a mean R² exceeding 0.87, confirming its effectiveness in capturing diurnal FRP variability. However, significant differences in diurnal patterns were observed across regions and vegetation types. Region 1 exhibited relatively lower fire intensity but still displayed clear unimodal diurnal patterns, peaking from morning to midday (local time), possibly related to agricultural practices or sustained peatland fires. Region 2 displayed pronounced afternoon peaks, particularly evident in grassland ($R^2 = 0.98$). In Regions 3 and 4, cropland, forest, and grassland showed excellent fitting performance ($R^2 \ge 0.91$), reflecting distinct anthropogenic burning patterns. For instance, cropland fires in Northeast China exhibited clear unimodal diurnal cycles, predominantly concentrated between 9:00 and 16:00 local time. These Gaussian function-based climatological FRP diurnal cycles effectively characterize the typical diurnal fire variations across different regions and vegetation types, establishing essential groundwork for further developing dynamic gap-filling methods and improving the continuity and reliability of satellite-derived fire observations.

3.2.2 Dynamic adjustment and gap-filling of FRP diurnal cycles

To enhance the spatiotemporal accuracy and reliability of BB emission inventories in SEA, a regionally adaptive approach was developed for dynamic adjustment and climatological gap filling of FRP based on region-specific observational characteristics. Using long-term AHI observations, climatological diurnal FRP cycles were reconstructed and applied to representative fire events in 2023 across four key regions and five vegetation types (Figure 5). The Gaussian Least Squares (GLS) fitting consistently delivered robust performance across all regions and ecosystems, with coefficients of determination (R2) reaching up to 0.98, confirming the reliability and broad applicability of the method for daily-scale FRP reconstruction. In Region 1, cropland fires exhibited a distinct and well-captured morning peak (UTC 02:00-06:00, approximately 09:00-13:00 local time) that was well captured by the dynamic fitting, achieving high accuracy ($R^2 = 0.82$) and strong agreement between the fitted curves and observations. In Region 2, dynamic Gaussian fitting methods, including GLS and Gaussian Vertical Movement (GVM), substantially outperformed conventional climatological fitting, underscoring their advantage in reproducing actual fire behavior. Regions 3 and 4 also demonstrated strong fitting results for forest and grassland fires, reflecting highly regular diurnal fire patterns and the effectiveness of dynamic parameter adjustment in identifying peak burning periods. Notably, in Northeast China, all vegetation types except grasslands, which lacked sufficient observations for fitting, exhibited the highest fitting performance (R² ≥ 0.8), with cropland fires showing a clearly defined unimodal diurnal pattern. This reflects the influence of well-regulated anthropogenic burning activities, such as crop residue combustion, or seasonally managed fire regimes during official fire prevention periods, underscoring the strong temporal

396

397

398

399

400

401

402

403

404

405 406

407

408

409

410 411

412

413

414

415

416

417

418

419

420

421

422 423

424

425

426

427

428

429

430

431

432

433 434

435 436





regularity of fires in this region and further validating the reliability of the proposed approach.

The dynamic gap-filling algorithm substantially improved both the temporal continuity and quantitative accuracy of FRP diurnal cycles, effectively mitigating observational deficiencies caused by cloud contamination and the spatiotemporal sampling limitations of satellite-based fire detection (Figure 6). Across all regions and vegetation types, reconstructed FRP profiles showed marked enhancements, particularly during key burning periods underrepresented in the original observations. In Region 1, cropland fires exhibited pronounced morning peaks (08:00-12:00 local time), with FRP increased by 67.7% after reconstruction, consistent with the common practice of morning crop residue burning. Shrubland fires in the same region showed a maximum enhancement of 80.6%, indicating active morning burning in tropical shrublands that was systematically underdetected in the original data. In Region 2, cropland FRP peaks during the afternoon and early evening (14:00-20:00 local time) increased by 74.2%, reflecting traditional afternoon burning practices, while overall FRP corrections were greater than in other regions. Forest fires in this region showed a 53.9% enhancement between 12:00 and 14:00, and grassland fires increased by 68.5% between 12:00 and 18:00, both highlighting intensified daytime combustion under dry conditions. In Region 3, forest and shrubland fires exhibited the highest enhancements, reaching up to 82.4%, whereas peatland fires had the lowest adjustments (25.4%), consistent with their stable smoldering characteristics and weak diurnal variability. In Region 4, shrubland FRP increased by 88.7% during 16:00-00:00 local time, revealing active evening-to-night burning that was systematically underestimated due to twilight detection gaps, with cropland fires showing the largest absolute increase (approximately 1 × 10⁶ W m⁻¹). Overall, the dynamically adjusted FRP profiles exhibited markedly improved temporal continuity compared with the original observations, capturing the primary peaks of fire activity and recovering missing signals during under-sampled periods, particularly for long-duration events (\geq 3 h), thereby providing a more accurate temporal representation essential for high-resolution emission modeling and atmospheric transport simulations.

Figure 7 compares the mean daily FRP distributions across SEA in 2023 under three scenarios: (a) the dynamic adjustment and gap-filling method, (b) the original observations without Gaussian fitting, and (c) conventional Gaussian fitting. The original observations systematically underestimate FRP due to cloud contamination, low temporal sampling frequency, and twilight detection blind zones. This underestimation is evident across all key regions, with low regional mean FRP values (21.34 MW in Region 1, 23.04 MW in Region 2, and 17.21 MW in Regions 3-4) and large standard deviations, indicating high spatiotemporal variability and missing peak fire activity (Figure 7 (b)). While the Gaussian fitting method improves spatial completeness by reconstructing climatological FRP diurnal curves, it neglects actual temporal fire dynamics, resulting in systematic overestimation in certain regions. For example, Region 2 showed a 2.17% increase in FRP relative to the original observations (23.35 MW), primarily due to artificial amplification during inactive periods (Figure 7 (c)). In contrast, the dynamically adjusted method incorporates region- and vegetation-specific diurnal characteristics, such as cropland burning peaks in the afternoon and shrubland fires occurring during twilight hours, leading to more realistic and continuous reconstructions. The dynamically fitted FRP showed improved regional means (e.g., 23.85 MW in Region 2 and 17.49 MW in Region 4), representing relative increases of 3.52% and 1.62% compared to the original data. In addition, the dynamic method effectively recovers underdetected fire signals, particularly in Regions 2 and 4 (0.81 MW and 0.23 MW, respectively), while also avoiding the overestimation seen in conventional Gaussian fitting methods (e.g., -0.51 MW in





- 437 Region 2). These results demonstrated that the proposed approach enhances both the accuracy and
- 438 representativeness of FRP spatial distributions by capturing realistic fire peaks and avoiding artificial
- 439 inflation during inactive hours, thus providing a more reliable input for high-resolution emission
- 440 modeling.

450

3.3 Comparison 2D BB with TROPOMI CO and five inventories

- 442 In this study, a top-down BB emission inventory for SEA was developed using a sequential conversion
- 443 framework (Eqs. 9-11) from FRP to fire radiative energy (FRE), dry matter (DM) consumption, and
- 444 ultimately to pollutant emissions. The FRP input was obtained from dynamically reconstructed diurnal
- 445 cycles (with enhanced spatiotemporal continuity). FRE was calculated by integrating the hourly FRP
- 446 series, providing a quantitative measure of total fire energy release. DM consumption was estimated from
- 447 FRE using a biomass combustion coefficient of 0.453 ± 0.068 kg MJ⁻¹. Pollutant emissions, including
- 448 CO₂, CO, nitrogen oxides (NO_x), PM_{2.5}, organic carbon (OC), and BC, among others, were subsequently
- 449 calculated by applying vegetation-specific emission factors (EFs, Table 2).

3.3.1 Satellite-based evaluation of SEAF CO emissions

- 451 Figure S5 displays the monthly mean distribution of CO column concentrations retrieved from
- 452 TROPOMI over SEA for 2023, revealing a pronounced seasonal enhancement during the spring burning
- 453 season (March-April). Notably elevated values, exceeding 0.08 mol m⁻², are observed over northern
- 454 Myanmar, northern Thailand, and western Laos. In comparison, Figure 8 (b-m) shows the monthly mean
- 455 CO emissions derived from the SEAF inventory, which exhibit remarkably consistent spatial and
- 456 temporal patterns with the satellite observations. The Region 2 shows a distinct emission peak during
- March and April, with maximum hourly emissions exceeding 0.8×10^6 g h⁻¹, closely matching the spatial
- 458 extent and intensity of TROPOMI-observed CO enhancements. Moreover, SEAF emissions also
- 459 captured the temporal evolution of CO concentrations with high fidelity. The monthly SEAF-derived CO
- emissions in Region 2 exhibit a strong linear correlation with TROPOMI CO column densities (R = 0.97)
- in Figure 8 (a). Both datasets reflect a coherent seasonal trend: a progressive increase from January to
- March, a clear peak in March, followed by a substantial decline through September, and a modest
- 463 rebound toward the end of the year. Importantly, the SEAF inventory not only reproduced the seasonal
- 464 variability but also successfully captured the precise timing and magnitude of the peak fire season.
- To assess the accuracy of the SEAF inventory at the event scale, a representative BB episode that
- 466 occurred on 9 March 2023 was examined using multi-source satellite data (Figure 9). The fire location
- 467 and associated smoke plume evolution were clearly captured by VIIRS (Figure 9 (a)) and time-resolved
- Himawari-9 true-color imagery (Figure 9 (c-n)), with red markers indicating active fire pixels.
- 469 Corresponding CO emissions were quantified from both TROPOMI satellite retrievals and the SEAF
- 470 inventory (Figure 9 (b)). The SEAF-derived CO emissions for this event totaled 0.307 Gg, closely
- 471 aligning with the TROPOMI-based estimate of 0.283 Gg. The relative deviation of 7.81% was well
- 472 within the \leq 10% random error margin defined for the TROPOMI CO product (Martínez-Alonso et al.,
- 473 2020), demonstrating the inventory's strong capacity to reproduce fire-induced emissions from individual
- 474 events with high accuracy.

475

3.3.2 Comparison of SEAF-derived PM_{2.5} with five existing BB inventories

476 To evaluate the reliability of PM_{2.5} emissions estimated by the SEAF inventory, a quantitative comparison

478

479 480

481 482

483 484

485

486

487

488

489

490

491

492

493

494

495

496

497

498

499

500

501

502

503

504





was performed against five widely used BB emission inventories (GFAS, FINN, FEER, QFED, and IS4FIRES). The SEAF inventory showed a total annual PM_{2.5} emission of 2362 Gg yr⁻¹ over SEA in 2023, which lies near the midpoint among the values given by the selected inventories in Figure 10 (a). This value is substantially lower than that of FINN v2.5.1 (7099 Gg yr⁻¹), which has been shown to overestimate BB emissions in this region (Jin et al., 2024). Relative to FINN, SEAF reduced the estimated emissions by approximately 66.7%. Emission estimates from SEAF closely aligned with those of FEER v1.0 (2335 Gg yr⁻¹) and QFED v2.6r1 (2345 Gg yr⁻¹), suggested that the SEAF estimates are constrained and consistent with other satellite-derived products. Moreover, SEAF showed strong consistency with FEER and QFED in Regions 1 and 2. In contrast, FINN consistently produces higher estimates, with the largest discrepancy in Region 2, where its emissions are nearly four times those of SEAF (Figure 10 (b-e)). Notably, SEAF also excelled in capturing the seasonal variability of PM_{2.5} emissions (Figure S6). In Region 2, emissions peak during March and April, reaching approximately 500 Gg month⁻¹, consistent with dry-season fire activity. This peak was reproduced by SEAF through a dynamic diurnal gap-filling approach that reconstructs temporal fire intensity patterns. GFAS and FEER underestimated the seasonal maximum, while FINN overestimated emissions and did not accurately reflect seasonal trends.

Regarding spatial distribution, SEAF accurately delineated key emission hotspots over northern Myanmar, northern Thailand, and western Laos (Figure 11), showed strong agreement with observed CO column enhancements from TROPOMI. In contrast, GFAS and FEER generated more spatially diffuse and inconsistent patterns, while FINN tended to overestimate both the magnitude and spatial extent of emissions across SEA. Spatial resolution also contributed significantly to inventory performance (Figure S7). SEAF (3 km) and FINN (1 km) provided finer-scale spatial detail compared to the coarser 10 km resolution of GFAS, QFED, FEER, and IS4FIRES. SEAF demonstrated enhanced spatial fidelity, effectively capturing localized emission hotspots and surface heterogeneity, including water bodies and bare land, particularly in topographically complex regions. While FINN showed similarly fine spatial resolution, it frequently overestimated emissions across various regions, resulting in higher total emissions and exaggerated spatial coverage. In contrast, coarse-resolution inventories smooth localized features, potentially obscuring critical emission signals.

3.4 Prediction of smoke plume height

505 506 Figure 12 (a) presents the SPH predicted by the RF model, demonstrating a high overall consistency with the MISR observations ($R^2 = 0.9$, RMSE = 334.68 m). Predictions falling within the reasonable range 507 (defined as "Good", with a bias within ±500 m) accounted for 90.6% of the RF model results. In contrast, 508 509 the traditional IS4FIRES achieved predictions within the "Good" range for only 57% of cases, while the PRM scheme commonly employed in air quality models performed even lower, at merely 44% (Rémy 510 511 et al., 2017). Furthermore, the RMSE values for the traditional models were significantly higher, at 533 m and 955 m, respectively, compared to the 334.68 m RMSE of the RF model developed in this study. 512 513 These results collectively indicate a substantial advantage of the present machine learning approach for 514 predicting SPH.

515 SHAP analysis was applied to interpret the contribution of environmental variables to SPH predictions, 516 providing insights into both the magnitude and direction of each factor's influence. The SHAP value sign

517 indicates whether a variable positively or negatively affects SPH, while color represents the variable's

519

520 521

522

523

524

525

526

527

528

529

530

531532

533

534

535

536

537

538

539

540

541

542

543





magnitude (red for high, blue for low). Temperature- and radiation-related variables emerged as the dominant drivers (Figure 12 (b)), consistent with previous findings that atmospheric temperature governs the buoyant transport of BB plumes (Feng et al., 2024; Freitas et al., 2007; Val Martin et al., 2010). In particular, the vertical integral of temperature (Vit) was the most significant factor, capturing the effect of atmospheric thermal structure on plume rise: larger vertical temperature gradients provide greater buoyant energy, leading to higher injection altitudes. Terrain elevation (z) was also identified as a key factor, as elevated regions promote stronger localized convection, especially in topographically complex areas like SEA. Longitude demonstrated high importance as well, reflecting the east-west climatic and geographic heterogeneity that significantly influences plume dynamics. Other notable variables included surface solar radiation (ssr), month, and latitude. Previous studies (Cohen et al., 2018; Feng et al., 2024; Holanda et al., 2023) have shown that seasonal variations in surface heating and fire activity during dry periods can enhance plume rise. The RF-SHAP model further revealed that these seasonal variables interact in a complex and nonlinear manner, particularly involving month, solar radiation, surface heating, and fire intensity. This intricate interplay helps explain why traditional models tend to perform poorly in regions characterized by strong seasonal variability. Additional factors such as planetary boundary layer height (blh), 10 m wind speed (v10), and FRP also contributed substantially. Higher FRP increases the mechanical energy available for vertical transport, while elevated PBL height offers a channel for plume penetration into the free troposphere. Importantly, SHAP analysis revealed that the influence of FRP is highly dependent on meteorological conditions, exhibiting strong nonlinear relationships that are often oversimplified in traditional models such as PRM. Although variables such as near-surface humidity (d2m), vegetation index (lai hv), and sensible heat flux (sshf) played relatively minor roles compared to dominant predictors, they still contributed meaningful information related to aerosol microphysics, fuel availability, and surface energy exchange. The RF-SHAP framework effectively integrates these nonlinear and region-dependent factors, providing a more comprehensive and interpretable alternative to conventional plume-rise schemes.

3.5 3D Biomass Burning inventory assessment

- Based on the previously constructed 2D SEAF inventory and SPH derived from the RF-SHAP model, a
- 545 high-resolution 3D BB emission inventory (3D SEAF) was constructed in this study. Vertical allocation
- 546 followed the approach proposed by the Texas Commission on Environmental Quality and the five-layer
- 547 scheme of IS4FIRES (0.025km, 0.275km, 1.0km, 2.75km, and 5.5km) (Texas Commission on
- 548 Environmental Quality, 2022). This approach yields a vertically resolved PM_{2.5} emission dataset across
- 549 five altitude bands.
- 550 A comparison of monthly emissions from the 3D SEAF and IS4FIRES inventories (Figure 13) reveals
- 551 similar seasonal patterns, with both inventories capturing a pronounced peak in fire emissions during
- March and April. Both inventories show a pronounced vertical uplift during these months, reflecting the
- intense burning and consequent plume rise in the dry season. Notably, during the peak period (March-
- April), SEAF allocates less PM_{2.5} to the lowest layers (0.025 km and 0.275 km) than IS4FIRES, while
- substantially increasing emissions in the upper layers (2.75 km and 5.5 km). This suggests that IS4FIRES
- may underestimate upper-level emissions, whereas SEAF offers a distribution more consistent with
- 557 MISR-observed plume structures.
- 558 Figure 14 (a-e) illustrates the spatial distribution of 3D SEAF emissions across different vertical layers.



560

561562

563

564565

566567

568

569

570

571

572

573

574

575

576

577

578

579

580

581

582

583

584

585

586

587

588

589

590

591

592

593

594

595

596

597



At the lowest level (0.025 km), emission intensities are generally low, with pronounced hotspots primarily located in northern Myanmar, northern Thailand, and Laos, where values reach up to 0.4 g m ² yr⁻¹. With increasing altitude, particularly at 0.275 km and 1 km, emission intensities increase significantly, with peak values of approximately 1.6 g m⁻² yr⁻¹ observed across Region 2. As altitude increases further to 2.75 km and 5.5 km, emission hotspots become increasingly confined, and the spatial extent of high-emission areas is reduced. Although the emission intensity at 5.5 km decreases relative to lower layers, notable localized plumes persist, especially over northern Laos. These patterns underscore the characteristic vertical uplift of BB plumes, extending from the near-surface to the lower troposphere. Figure 14 (f) further compares the vertical frequency distribution of SEAF emissions with those from MISR, GFAS, IS4FIRES, and CALIPSO satellite observations across SEA. The SEAF inventory exhibits a strong peak in emission frequency below 1km, reaching a maximum relative frequency of ~0.7, followed by a rapid decline above 1 km. Nevertheless, SEAF still registers non-negligible emissions above 2.75 km, reflecting its ability to represent both surface-concentrated and elevated plume injection events. This vertical profile closely aligns with CALIPSO observations, which also reveal near-surface dominance in aerosol vertical structure. In contrast, MISR, GFAS, and IS4FIRES display a broader vertical distribution of emissions. Specifically, GFAS exhibits relatively high emission frequencies in the 3-5 km altitude range, while MISR and IS4FIRES maintain substantial emission fractions between 2.75 and 5.5 km. Although the SEAF inventory shows lower emission frequencies in the middle and upper atmospheric layers compared to these inventories, it still retains a persistent, albeit smaller, fraction of emissions at 5.5 km. Notably, this aligns well with the extended plume tails observed by CALIPSO and GFAS, indicating the SEAF inventory's ability to represent both the near-surface concentration of BB plumes and the occurrence of elevated smoke layers. Such performance is consistent with independent satellite observations and highlights the realistic representation of plume dynamics provided by the SEAF vertical allocation scheme.

4. Discussion

The SEAF BB emission inventory developed in this study advances spatiotemporal resolution, dynamic adjustment, and vertical distribution modeling. Cloud correction and cross-calibration between VIIRS and Himawari-8/9 reduce biases associated with cloud cover and revisit cycles, yet uncertainties remain under extreme meteorological conditions and at large satellite zenith angles where simple cloud-fraction metrics cannot fully capture fire variability (Wang et al., 2018; Xie et al., 2018). The reconstruction of FRP diurnal cycles through Gaussian fitting effectively addresses data gaps but assumes a unimodal daily pattern. This simplification does not always reflect BB activity in SEA, where agricultural burning, peatland fires, and anomalous climate events often produce bimodal or irregular temporal structures (Fan et al., 2023; Yin, 2020). Regarding peatland fires, we acknowledge the inherent limitation of the FRP-derived top-down approach in capturing emissions from deep smoldering combustion. While this study seeks to address this limitation by applying peatland-specific emission factors, a strategy that yields regional totals in broad agreement with other inventories, the potential for underestimation remains a key source of uncertainty (Fisher et al., 2020). Consequently, rapid fluctuations or emergent fire behaviors may be underestimated despite the application of dynamic adjustments.

For the vertical allocation, a RF-SHAP model trained with MISR plume heights, ERA5 meteorology, and FRP was used to predict SPH, which then guided a five-layer distribution scheme following the Texas Commission on Environmental Quality and IS4FIRES. This hybrid approach links data-driven





601 SPH prediction with a structured allocation framework and offers advantages over conventional plume-602 rise parameterizations. However, the coarse resolution of ERA5 together with the sparse sampling of MISR limit the representation of fine-scale convection and extreme lofting, resulting in potential 603 604 underestimation during localized outbreaks (Sessions et al., 2011; Val Martin et al., 2012). Compared with GFAS, FINN, FEER, QFED, and IS4FIRES, SEAF captures emission magnitudes and seasonal 605 variability more accurately, yet short-lived peaks and near-surface emissions remain underrepresented, 606 607 reflecting the emphasis on dominant injection layers rather than rare extreme events. Further 608 improvements will require higher-resolution meteorological fields, integration of additional 609 geostationary platforms such as Geostationary Environment Monitoring Spectrometer (GEMS) and 610 GOES-R, and complementary lidar observations (e.g., CALIPSO) to better constrain vertical injection 611 under extreme and under-sampled conditions.

5. Conclusion

612

- The SEAF emission inventory was developed as an hourly 3 km resolution 2D/3D dataset for 2023,
- 614 addressing deficiencies in diurnal profiles and vertical injection of BB emissions. The inventory
- 615 integrates cloud-corrected, cross-calibrated FRP from AHI and VIIRS with a region- and vegetation-
- 616 specific Gaussian reconstruction and dynamic gap filling, restoring missing peaks while minimizing
- artificial inflation. Validation against TROPOMI CO (R = 0.97) and independent estimates indicates high
- reliability, with annual PM_{2.5} emissions (2362 Gg) consistent with FEER and QFED and substantially
- lower than FINN. The vertical dimension is constrained through a RF-SHAP interpretation trained with
- MISR and ERA5, achieving an $R^2 = 0.90$ and an RMSE = 335 m, and reallocating injection from near
- surface layers toward 2.75 and 5.5 km during the spring burning peak in closer accordance with MISR and CALIPSO structures. These improvements in temporal completeness and vertical realism enhance
- the representation of BB emissions in chemical transport models, supporting more robust assessments of
- air quality, transboundary smoke transport, and radiative impacts in SEA.

625 Data Availability

- 626 The SEAF emission inventory developed in this study, including 2D/3D hourly products at 3 km
- 627 resolution for 2023, is publicly available at Zenodo (https://doi.org/10.5281/zenodo.16793129) (Jin et
- 628 al., 2025). Satellite datasets used include FRP from the AHI onboard Himawari-8/9 provided by the Japan
- 629 Meteorological Agency (JMA), FRP from the VIIRS onboard Suomi-NPP and NOAA-20 provided by
- NASA/NOAA, column carbon monoxide (CO) from the TROPOMI operated by the European Space
- 631 Agency (ESA), and plume height observations from the MISR provided by NASA. ERA5 meteorological
- 632 reanalysis data were obtained from the ECMWF. All datasets are openly accessible from their respective
- 633 providers.

634 Competing interests

The authors declare that they have no conflict of interest.

636 Acknowledgments

- 637 The authors gratefully acknowledge the Japan Meteorological Agency (JMA) for Himawari-8/9 AHI data,
- NASA/NOAA for VIIRS FRP products, the European Space Agency (ESA) for TROPOMI CO data,
- 639 NASA for MISR plume height observations, and the European Centre for Medium-Range Weather

https://doi.org/10.5194/essd-2025-515 Preprint. Discussion started: 21 October 2025 © Author(s) 2025. CC BY 4.0 License.





640	Forecasts (ECMWF) for ERA5 meteorological data. This work was supported by the Science and
641	Technology Program of Guangdong Province (Science and Technology Innovation Platform Category)
642	(Grant No. 2019B121201002), and the National Natural Science Foundation of China (Grant No.
643	42075181, 42375182, and 42175086). Innovation Group Project of Southern Marine Science and
644	Engineering Guangdong Laboratory (Zhuhai) (No. 311024001).





646 References

- Achtemeier, G. L., Goodrick, S. A., Liu, Y., Garcia-Menendez, F., Hu, Y., and Odman, M. T.: Modeling
- 648 smoke plume-rise and dispersion from southern united states prescribed burns with daysmoke,
- 649 Atmosphere, 2, 358–388, https://doi.org/10.3390/atmos2030358, 2011.
- 650 Agrawal, N., Nelson, P. V., and Low, R. D.: A novel approach for predicting large wildfires using machine
- 651 learning towards environmental justice via environmental remote sensing and atmospheric reanalysis
- data across the united states, Remote Sens., 15, 5501, https://doi.org/10.3390/rs15235501, 2023.
- 653 Andela, N., Kaiser, J. W., Van Der Werf, G. R., and Wooster, M. J.: New fire diurnal cycle
- 654 characterizations to improve fire radiative energy assessments made from MODIS observations, Atmos.
- 655 Chem. Phys., 15, 8831–8846, https://doi.org/10.5194/acp-15-8831-2015, 2015.
- 656 Andreae, M. O.: Emission of trace gases and aerosols from biomass burning an updated assessment,
- 657 Atmos. Chem. Phys., 19, 8523–8546, https://doi.org/10.5194/acp-19-8523-2019, 2019.
- 658 Bell, B., Hersbach, H., Simmons, A., Berrisford, P., Dahlgren, P., Horányi, A., Muñoz-Sabater, J., Nicolas,
- 659 J., Radu, R., Schepers, D., Soci, C., Villaume, S., Bidlot, J.-R., Haimberger, L., Woollen, J., Buontempo,
- 660 C., and Thépaut, J.-N.: The ERA5 global reanalysis: Preliminary extension to 1950, Quarterly Journal of
- the Royal Meteorological Society, 147, 4186–4227, https://doi.org/10.1002/qj.4174, 2021.
- Bessho, K., Date, K., Hayashi, M., Ikeda, A., Imai, T., Inoue, H., Kumagai, Y., Miyakawa, T., Murata,
- 663 H., Ohno, T., Okuyama, A., Oyama, R., Sasaki, Y., Shimazu, Y., Shimoji, K., Sumida, Y., Suzuki, M.,
- Taniguchi, H., Tsuchiyama, H., Uesawa, D., Yokota, H., and Yoshida, R.: An introduction to himawari-
- 665 8/9 Japan's new-generation geostationary meteorological satellites, J. Meteorol. Soc. Jpn., II, 94, 151–
- 666 183, https://doi.org/10.2151/jmsj.2016-009, 2016.
- 667 Borsdorff, T., Aan de Brugh, J., Hu, H., Aben, I., Hasekamp, O., and Landgraf, J.: Measuring carbon
- monoxide with TROPOMI: First results and a comparison with ECMWF-IFS analysis data, Geophys.
- Res. Lett., 45, 2826–2832, https://doi.org/10.1002/2018GL077045, 2018.
- 670 Borsdorff, T., Campos, T., Kille, N., Zarzana, K. J., Volkamer, R., and Landgraf, J.: Vertical information
- 671 of CO from TROPOMI total column measurements in context of the CAMS-IFS data assimilation
- 672 scheme, Atmos. Meas. Tech., 16, 3027–3038, https://doi.org/10.5194/amt-16-3027-2023, 2023.
- 673 Breiman, L.: Random forests, Mach. Learn., 45, 5–32, https://doi.org/10.1023/A:1010933404324, 2001.
- 674 Briggs, G. A.: Plume rise: A critical survey (TID-25075), Oak Ridge, https://doi.org/10.2172/4743102,
- 675 1969
- 676 Brown, P. T., Hanley, H., Mahesh, A., Reed, C., Strenfel, S. J., Davis, S. J., Kochanski, A. K., and
- 677 Clements, C. B.: Climate warming increases extreme daily wildfire growth risk in California, Nature,
- 678 621, 760–766, https://doi.org/10.1038/s41586-023-06444-3, 2023.
- 679 Chen, J., Li, R., Tao, M., Wang, L., Lin, C., Wang, J., Wang, L., Wang, Y., and Chen, L.: Overview of the
- 680 performance of satellite fire products in China: Uncertainties and challenges, Atmos. Environ., 268,
- 681 118838, https://doi.org/10.1016/j.atmosenv.2021.118838, 2022.
- 682 Chen, J., Lv, Q., Wu, S., Zeng, Y., Li, M., Chen, Z., Zhou, E., Zheng, W., Liu, C., Chen, X., Yang, J., and





- 683 Gao, B.: An adapted hourly himawari-8 fire product for China: Principle, methodology and verification,
- 684 Earth Syst. Sci. Data, 15, 1911–1931, https://doi.org/10.5194/essd-15-1911-2023, 2023.
- 685 Cohen, J. B., Ng, D. H. L., Lim, A. W. L., and Chua, X. R.: Vertical distribution of aerosols over the
- 686 Maritime Continent during El Niño, Atmospheric Chemistry and Physics, 18, 7095-7108,
- https://doi.org/10.5194/acp-18-7095-2018, 2018. 687
- Crutzen, P. J., Heidt, L. E., Krasnec, J. P., Pollock, W. H., and Seiler, W.: Biomass burning as a source of 688
- 689 atmospheric gases CO, H₂, N₂O, NO, CH₃Cl and COS, Nature, 282, 253-256,
- 690 https://doi.org/10.1038/282253a0, 1979.
- 691 Csiszar, I., Schroeder, W., Giglio, L., Ellicott, E., Vadrevu, K. P., Justice, C. O., and Wind, B.: Active
- 692 fires from the suomi NPP visible infrared imaging radiometer suite: product status and first evaluation
- 693 results, J. Geophys. Res.: Atmos., 119, 803-816, https://doi.org/10.1002/2013JD020453, 2014.
- 694 Dong, L., Leung, L. R., Qian, Y., Zou, Y., Song, F., and Chen, X.: Meteorological environments
- 695 associated with california wildfires and their potential roles in wildfire changes during 1984-2017, J.
- Geophys. Res.: Atmos., 126, e2020JD033180, https://doi.org/10.1029/2020JD033180, 2021. 696
- 697 Driscoll, D. A., Macdonald, K. J., Gibson, R. K., Doherty, T. S., Nimmo, D. G., Nolan, R. H., Ritchie, E.
- 698 G., Williamson, G. J., Heard, G. W., Tasker, E. M., Bilney, R., Porch, N., Collett, R. A., Crates, R. A.,
- 699 Hewitt, A. C., Pendall, E., Boer, M. M., Gates, J., Boulton, R. L., Mclean, C. M., Groffen, H., Maisey,
- 700 A. C., Beranek, C. T., Ryan, S. A., Callen, A., Hamer, A. J., Stauber, A., Daly, G. J., Gould, J., Klop-
- Toker, K. L., Mahony, M. J., Kelly, O. W., Wallace, S. L., Stock, S. E., Weston, C. J., Volkova, L., Black, 701
- 702 D., Gibb, H., Grubb, J. J., McGeoch, M. A., Murphy, N. P., Lee, J. S., Dickman, C. R., Neldner, V. J.,
- 703 Ngugi, M. R., Miritis, V., Köhler, F., Perri, M., Denham, A. J., Mackenzie, B. D. E., Reid, C. A. M.,
- Rayment, J. T., Arriaga-Jiménez, A., Hewins, M. W., Hicks, A., Melbourne, B. A., Davies, K. F., Bitters, 704 705 M. E., Linley, G. D., Greenville, A. C., Webb, J. K., Roberts, B., Letnic, M., Price, O. F., Walker, Z. C.,
- 706 Murray, B. R., Verhoeven, E. M., Thomsen, A. M., Keith, D., Lemmon, J. S., Ooi, M. K. J., Allen, V. L., 707
- Decker, O. T., Green, P. T., Moussalli, A., Foon, J. K., Bryant, D. B., Walker, K. L., Bruce, M. J., Madani,
- 708 G., Tscharke, J. L., Wagner, B., Nitschke, C. R., Gosper, C. R., Yates, C. J., Dillon, R., Barrett, S., Spencer,
- 709 E. E., Wardle, G. M., Newsome, T. M., Pulsford, S. A., Singh, A., Roff, A., Marsh, K. J., Mcdonald, K.,
- 710 Howell, L. G., Lane, M. R., Cristescu, R. H., Witt, R. R., et al.: Biodiversity impacts of the 2019-2020
- 711 Australian megafires, Nature, 635, 898-905, https://doi.org/10.1038/s41586-024-08174-6, 2024.
- 712 Ekanayake, I. U., Meddage, D. P. P., and Rathnayake, U.: A novel approach to explain the black-box
- 713 nature of machine learning in compressive strength predictions of concrete using shapley additive
- 714 explanations (SHAP), Case Stud. Constr. Mater., 16, e01059,
- 715 https://doi.org/10.1016/j.cscm.2022.e01059, 2022.
- Fan, H., Yang, X., Zhao, C., Yang, Y., and Shen, Z.: Spatiotemporal variation characteristics of global 716
- 717 fires and their emissions, Atmospheric Chemistry and Physics, 23, 7781-7798,
- 718 https://doi.org/10.5194/acp-23-7781-2023, 2023.
- 719 Feng, X., Mickley, L. J., Bell, M. L., Liu, T., Fisher, J. A., and Val Martin, M.: Improved estimates of
- 720 smoke exposure during Australia fire seasons: importance of quantifying plume injection heights,
- 721 Atmospheric Chemistry and Physics, 24, 2985-3007, https://doi.org/10.5194/acp-24-2985-2024, 2024.





- 722 Ferrero, E., Alessandrini, S., Anderson, B., Tomasi, E., Jimenez, P., and Meech, S.: Lagrangian
- 723 simulation of smoke plume from fire and validation using ground-based lidar and aircraft measurements,
- 724 Atmos. Environ., 213, 659–674, https://doi.org/10.1016/j.atmosenv.2019.06.049, 2019.
- 725 Fisher, D., Wooster, M. J., Xu, W., Thomas, G., and Lestari, P.: Top-Down Estimation of Particulate
- 726 Matter Emissions from Extreme Tropical Peatland Fires Using Geostationary Satellite Fire Radiative
- 727 Power Observations, Sensors, 20, 7075, https://doi.org/10.3390/s20247075, 2020.
- 728 Freeborn, P. H., Wooster, M. J., Hao, W. M., Ryan, C. A., Nordgren, B. L., Baker, S. P., and Ichoku, C.:
- 729 Relationships between energy release, fuel mass loss, and trace gas and aerosol emissions during
- 730 laboratory biomass fires, J. Geophys. Res.: Atmos., 113, 2007JD008679,
- 731 https://doi.org/10.1029/2007JD008679, 2008.
- 732 Freitas, S. R., Longo, K. M., Chatfield, R., Latham, D., Silva Dias, M. A. F., Andreae, M. O., Prins, E.,
- 733 Santos, J. C., Gielow, R., and Carvalho, J. A.: Including the sub-grid scale plume rise of vegetation fires
- 734 in low resolution atmospheric transport models, Atmos. Chem. Phys., 7, 3385-3398,
- 735 https://doi.org/10.5194/acp-7-3385-2007, 2007.
- 736 Giglio, L., Van Der Werf, G. R., Randerson, J. T., Collatz, G. J., and Kasibhatla, P.: Global estimation of
- 737 burned area using MODIS active fire observations, Atmos. Chem. Phys., 6, 957-974,
- 738 https://doi.org/10.5194/acp-6-957-2006, 2006.
- 739 Giglio, L., Schroeder, W., and Justice, C. O.: The collection 6 MODIS active fire detection algorithm and
- 740 fire products, Remote Sens. Environ., 178, 31–41, https://doi.org/10.1016/j.rse.2016.02.054, 2016.
- Gkatzelis, G. I., Coggon, M. M., Stockwell, C. E., Hornbrook, R. S., Allen, H., Apel, E. C., Bela, M. M.,
- 742 Blake, D. R., Bourgeois, I., Brown, S. S., Campuzano-Jost, P., St. Clair, J. M., Crawford, J. H., Crounse,
- J. D., Day, D. A., DiGangi, J. P., Diskin, G. S., Fried, A., Gilman, J. B., Guo, H., Hair, J. W., Halliday, H.
- 744 S., Hanisco, T. F., Hannun, R., Hills, A., Huey, L. G., Jimenez, J. L., Katich, J. M., Lamplugh, A., Lee,
- 745 Y. R., Liao, J., Lindaas, J., McKeen, S. A., Mikoviny, T., Nault, B. A., Neuman, J. A., Nowak, J. B.,
- 746 Pagonis, D., Peischl, J., Perring, A. E., Piel, F., Rickly, P. S., Robinson, M. A., Rollins, A. W., Ryerson,
- 747 T. B., Schueneman, M. K., Schwantes, R. H., Schwarz, J. P., Sekimoto, K., Selimovic, V., Shingler, T.,
- 748 Tanner, D. J., Tomsche, L., Vasquez, K. T., Veres, P. R., Washenfelder, R., Weibring, P., Wennberg, P. O.,
- Wisthaler, A., Wolfe, G. M., Womack, C. C., Xu, L., Ball, K., Yokelson, R. J., and Warneke, C.:
- 750 Parameterizations of US wildfire and prescribed fire emission ratios and emission factors based on
- 751 FIREX-AQ aircraft measurements, Atmos. Chem. Phys., 24, 929-956, https://doi.org/10.5194/acp-24-
- 752 929-2024, 2024.
- 753 Griffin, D., Chen, J., Anderson, K., Makar, P., McLinden, C. A., Dammers, E., and Fogal, A.: Biomass
- 754 burning CO emissions: Exploring insights through TROPOMI-derived emissions and emission
- 755 coefficients, Atmos. Chem. Phys., 24, 10159–10186, https://doi.org/10.5194/acp-24-10159-2024, 2024.
- 756 Haugen, D. A.: Lectures on air pollution and environmental impact analyses, American Meteorological
- 757 Society, Boston, MA, https://doi.org/10.1007/978-1-935704-23-2, 1982.
- Holanda, B. A., Franco, M. A., Walter, D., Artaxo, P., Carbone, S., Cheng, Y., Chowdhury, S., Ditas, F.,
- 759 Gysel-Beer, M., Klimach, T., Kremper, L. A., Krüger, O. O., Lavric, J. V., Lelieveld, J., Ma, C., Machado,
- 760 L. A. T., Modini, R. L., Morais, F. G., Pozzer, A., Saturno, J., Su, H., Wendisch, M., Wolff, S., Pöhlker,





- 761 M. L., Andreae, M. O., Pöschl, U., and Pöhlker, C.: African biomass burning affects aerosol cycling over
- 762 the Amazon, Commun Earth Environ, 4, 154, https://doi.org/10.1038/s43247-023-00795-5, 2023.
- 763 Huang, H., Jin, Y., Sun, W., Gao, Y., Sun, P., and Ding, W.: Biomass burning in northeast China over two
- 764 decades: Temporal trends and geographic patterns, Remote Sens., 16, 1911,
- 765 https://doi.org/10.3390/rs16111911, 2024.
- 766 Jang, E., Kang, Y., Im, J., Lee, D.-W., Yoon, J., and Kim, S.-K.: Detection and monitoring of forest fires
- 767 using himawari-8 geostationary satellite data in south korea, Remote Sens., 11, 271,
- 768 https://doi.org/10.3390/rs11030271, 2019.
- 769 JAXA/EORC: Himawari-8 Wildfire Hotspot Data, 2020.
- 770 Jin, Y., Liu, Y., Lu, X., Chen, X., Shen, A., Wang, H., Cui, Y., Xu, Y., Li, S., Liu, J., Zhang, M., Ma, Y.,
- 771 and Fan, Q.: Measurement report: Assessing the impacts of emission uncertainty on aerosol optical
- 772 properties and radiative forcing from biomass burning in peninsular Southeast Asia, Atmospheric
- 773 Chemistry and Physics, 24, 367–395, https://doi.org/10.5194/acp-24-367-2024, 2024.
- 774 Jin, Y., Huang, H., Liu, J., Liu, Y., Chen, X., Chen, Y., Li, L., and Fan, Q.: Three-Dimensional Biomass
- 775 Burning Emission Inventory for Southeast and East Asia Based on Multi-Source Data and Machine
- 776 Learning (1.0), https://doi.org/10.5281/ZENODO.16793128, 2025.
- 777 Jong, H. N.: As fires ravaged Indonesia in 2023, some positive trends emerged, data show, Mongabay
- 778 News, 9th April, 2024.
- Ke, Z., Wang, Y., Zou, Y., Song, Y., and Liu, Y.: Global wildfire plume-rise data set and parameterizations
- 780 for climate model applications, J. Geophys. Res.: Atmos., 126, e2020JD033085,
- 781 https://doi.org/10.1029/2020JD033085, 2021.
- 782 Kim, S. Y., Jun, C., and Na, W.: Ensemble-based forecasting of wildfire potentials using relative index
- 783 in gangwon province, south korea, Ecol. Inform., 86, 103021,
- 784 https://doi.org/10.1016/j.ecoinf.2025.103021, 2025.
- 785 Koster, R. D., Darmenov, A. S., and da Silva, A. M.: The quick fire emissions dataset (QFED):
- 786 documentation of versions 2.1, 2.2 and 2.4: technical report series on global modeling and data
- 787 assimilation volume 38, NASA Goddard Space Flight Center, 2015.
- 788 Landgraf, J., de Brugh, J. A., Scheepmaker, R., Borsdorff, T., Houweling, S., and Hasekamp, O.:
- 789 Algorithm theoretical baseline document for sentinel-5 precursor: Carbon monoxide total column
- retrieval, Neth. Inst. Space Res. Neth. SRON-S5P-LEV2-RP-002, 2018.
- 791 Li, F., Zhang, X., Roy, D. P., and Kondragunta, S.: Estimation of biomass-burning emissions by fusing
- 792 the fire radiative power retrievals from polar-orbiting and geostationary satellites across the
- 793 conterminous United States, Atmos. Environ., 211, 274-287,
- 794 https://doi.org/10.1016/j.atmosenv.2019.05.017, 2019.
- 795 Li, F., Zhang, X., Kondragunta, S., Lu, X., Csiszar, I., and Schmidt, C. C.: Hourly biomass burning
- 796 emissions product from blended geostationary and polar-orbiting satellites for air quality forecasting
- 797 applications, Remote Sens. Environ., 281, 113237, https://doi.org/10.1016/j.rse.2022.113237, 2022.





- 798 Li, Y., Tong, D., Ma, S., Freitas, S. R., Ahmadov, R., Sofiev, M., Zhang, X., Kondragunta, S., Kahn, R.,
- 799 Tang, Y., Baker, B., Campbell, P., Saylor, R., Grell, G., and Li, F.: Impacts of estimated plume rise on
- 800 PM_{2.5} exceedance prediction during extreme wildfire events: a comparison of three schemes (Briggs,
- 801 Freitas, and Sofiev), Atmos. Chem. Phys., 23, 3083-3101, https://doi.org/10.5194/acp-23-3083-2023,
- 802 2023.
- Liu, J., Cohen, J. B., He, Q., Tiwari, P., and Qin, K.: Accounting for NOx emissions from biomass burning
- 804 and urbanization doubles existing inventories over South, Southeast and East Asia, Commun Earth
- 805 Environ, 5, 255, https://doi.org/10.1038/s43247-024-01424-5, 2024a.
- 806 Liu, J., Cohen, J. B., Tiwari, P., Liu, Z., Yim, S. H.-L., Gupta, P., and Qin, K.: New top-down estimation
- 807 of daily mass and number column density of black carbon driven by OMI and AERONET observations,
- 808 Remote Sensing of Environment, 315, 114436, https://doi.org/10.1016/j.rse.2024.114436, 2024b.
- 809 Liu, M. and Popescu, S.: Estimation of biomass burning emissions by integrating ICESat-2, Landsat 8,
- 810 and Sentinel-1 data, Remote Sens. Environ., 280, 113172, https://doi.org/10.1016/j.rse.2022.113172,
- 811 2022.
- 812 López-Noreña, A. I., Berná, L., Tames, M. F., Millán, E. N., Puliafito, S. E., and Fernandez, R. P.:
- 813 Influence of emission inventory resolution on the modeled spatio-temporal distribution of air pollutants
- 814 in buenos aires, argentina, using WRF-chem, Atmos. Environ., 269, 118839,
- 815 https://doi.org/10.1016/j.atmosenv.2021.118839, 2022.
- 816 Mangalathu, S., Hwang, S.-H., and Jeon, J.-S.: Failure mode and effects analysis of RC members based
- on machine-learning-based SHapley additive exPlanations (SHAP) approach, Eng. Struct., 219, 110927,
- 818 2020
- 819 Martínez-Alonso, S., Deeter, M., Worden, H., Borsdorff, T., Aben, I., Commane, R., Daube, B., Francis,
- 820 G., George, M., Landgraf, J., Mao, D., McKain, K., and Wofsy, S.: 1.5 years of TROPOMI CO
- 821 measurements: comparisons to MOPITT and ATom, Atmos. Meas. Tech., 13, 4841-4864,
- 822 https://doi.org/10.5194/amt-13-4841-2020, 2020.
- 823 Nastan, A., Val, S., Ainsworth, H., Tosca, M., Galvin, A., Boone, J., Nair, P., Virdi, M., and Garay, M.:
- 824 User Guide: The MISR Enhanced Research and Lookup Interface (MERLIN) (JPL D-108271), Jet
- Propulsion Laboratory, California Institute of Technology, 2022.
- 826 Nelson, D., Garay, M., Kahn, R., and Dunst, B.: Stereoscopic height and wind retrievals for aerosol
- 827 plumes with the MISR INteractive eXplorer (MINX), Remote Sens., 5, 4593-4628,
- 828 https://doi.org/10.3390/rs5094593, 2013.
- 829 Nguyen, H. M., He, J., and Wooster, M. J.: Biomass burning CO, PM and fuel consumption per unit
- 830 burned area estimates derived across Africa using geostationary SEVIRI fire radiative power and
- 831 Sentinel-5P CO data, Atmos. Chem. Phys., 23, 2089–2118, https://doi.org/10.5194/acp-23-2089-2023,
- 832 2023.
- 833 Pullabhotla, H. K., Zahid, M., Heft-Neal, S., Rathi, V., and Burke, M.: Global biomass fires and infant
- 834 mortality, Proc. Natl. Acad. Sci., 120, e2218210120, https://doi.org/10.1073/pnas.2218210120, 2023.
- 835 Reining, S., Wussow, M., Zanocco, C., and Neumann, D.: Roof renewal disparities widen the equity gap





- in residential wildfire protection, Nat. Commun., 16, 463, https://doi.org/10.1038/s41467-024-55705-w,
- 837 2025.
- 838 Rémy, S., Veira, A., Paugam, R., Sofiev, M., Kaiser, J. W., Marenco, F., Burton, S. P., Benedetti, A.,
- 839 Engelen, R. J., Ferrare, R., and Hair, J. W.: Two global data sets of daily fire emission injection heights
- since 2003, Atmos. Chem. Phys., 17, 2921–2942, https://doi.org/10.5194/acp-17-2921-2017, 2017.
- 841 Schroeder, W., Oliva, P., Giglio, L., and Csiszar, I. A.: The new VIIRS 375m active fire detection data
- 842 product: algorithm description and initial assessment, Remote Sens. Environ., 143, 85-96,
- 843 https://doi.org/10.1016/j.rse.2013.12.008, 2014.
- 844 Schroeder, W., Giglio, L., and Hall, J.: Collection 2 visible infrared imaging radiometer suite (VIIRS)
- 845 375-m active fire product user's guide, National Oceanic and Atmospheric Administration (NOAA),
- 846 National Environmental Satellite, Data, and Information Service (NESDIS); Department of Geographical
- 847 Sciences, University of Maryland, 2024.
- 848 Sessions, W. R., Fuelberg, H. E., Kahn, R. A., and Winker, D. M.: An investigation of methods for
- 849 injecting emissions from boreal wildfires using WRF-Chem during ARCTAS, Atmospheric Chemistry
- and Physics, 11, 5719–5744, https://doi.org/10.5194/acp-11-5719-2011, 2011.
- 851 Sofiev, M., Vankevich, R., Lotjonen, M., Prank, M., Petukhov, V., Ermakova, T., Koskinen, J., and
- 852 Kukkonen, J.: An operational system for the assimilation of the satellite information on wild-land fires
- for the needs of air quality modelling and forecasting, Atmos. Chem. Phys., 9, 6833-6847,
- https://doi.org/10.5194/acp-9-6833-2009, 2009.
- 855 Sofiev, M., Ermakova, T., and Vankevich, R.: Evaluation of the smoke-injection height from wild-land
- 856 fires using remote-sensing data, Atmos. Chem. Phys., 12, 1995–2006, https://doi.org/10.5194/acp-12-
- 857 1995-2012, 2012.
- 858 Texas Commission on Environmental Quality: Develop tools to process and evaluate options for
- 859 improved fire emission inventories (EIs), Texas Commission on Environmental Quality and Ramboll US
- 860 Consulting, Inc., 2022.
- 861 Üstek, İ., Arana-Catania, M., Farr, A., and Petrunin, I.: Deep autoencoders for unsupervised anomaly
- 862 detection in wildfire prediction, Earth Space Sci., 11, e2024EA003997,
- 863 https://doi.org/10.1029/2024EA003997, 2024.
- Val Martin, M., Logan, J. A., Kahn, R. A., Leung, F.-Y., Nelson, D. L., and Diner, D. J.: Smoke injection
- 865 heights from fires in North America: analysis of 5 years of satellite observations, Atmospheric Chemistry
- and Physics, 10, 1491–1510, https://doi.org/10.5194/acp-10-1491-2010, 2010.
- 867 Val Martin, M., Kahn, R. A., Logan, J. A., Paugam, R., Wooster, M., and Ichoku, C.: Space-based
- 868 observational constraints for 1-D fire smoke plume-rise models, J. Geophys. Res., 117, 2012JD018370,
- 869 https://doi.org/10.1029/2012JD018370, 2012.
- 870 Val Martin, M., Kahn, R. A., and Tosca, M. G.: A global analysis of wildfire smoke injection heights
- 871 derived from space-based multi-angle imaging, Remote Sens., 10, 1609
- 872 https://doi.org/10.3390/rs10101609, 2018.





- 873 Vermote, E., Ellicott, E., Dubovik, O., Lapyonok, T., Chin, M., Giglio, L., and Roberts, G. J.: An
- 874 approach to estimate global biomass burning emissions of organic and black carbon from MODIS fire
- 875 radiative power, J. Geophys. Res.: Atmos., 114, 2008JD011188, https://doi.org/10.1029/2008JD011188,
- 876 2009.
- 877 Vitolo, C., Di Giuseppe, F., Barnard, C., Coughlan, R., San-Miguel-Ayanz, J., Libertá, G., and
- 878 Krzeminski, B.: ERA5-based global meteorological wildfire danger maps, Sci. Data, 7, 216,
- 879 https://doi.org/10.1038/s41597-020-0554-z, 2020.
- 880 Wang, J., Yue, Y., Wang, Y., Ichoku, C., Ellison, L., and Zeng, J.: Mitigating satellite-based fire sampling
- 881 limitations in deriving biomass burning emission rates: application to WRF-chem model over the
- 882 northern sub-saharan african region, J. Geophys. Res.: Atmos., 123, 507-528,
- 883 https://doi.org/10.1002/2017JD026840, 2018.
- Wang, S. S.-C. and Wang, Y.: Quantifying the effects of environmental factors on wildfire burned area
- in the south central US using integrated machine learning techniques, Atmos. Chem. Phys., 20, 11065–
- 886 11087, https://doi.org/10.5194/acp-20-11065-2020, 2020.
- 887 Wooster, M. J., Roberts, G., Perry, G. L. W., and Kaufman, Y. J.: Retrieval of biomass combustion rates
- 888 and totals from fire radiative power observations: FRP derivation and calibration relationships between
- biomass consumption and fire radiative energy release, J. Geophys. Res.: Atmos., 110, 2005JD006318,
- 890 https://doi.org/10.1029/2005JD006318, 2005.
- 891 Xie, Z., Song, W., Ba, R., Li, X., and Xia, L.: A Spatiotemporal Contextual Model for Forest Fire
- 892 Detection Using Himawari-8 Satellite Data, Remote Sensing, 10, 1992,
- 893 https://doi.org/10.3390/rs10121992, 2018.
- 894 Xu, G. and Zhong, X.: Real-time wildfire detection and tracking in australia using geostationary satellite:
- 895 Himawari-8, Remote Sens. Lett., 8, 1052–1061, https://doi.org/10.1080/2150704X.2017.1350303, 2017.
- 896 Xu, Y., Huang, Z., Ou, J., Jia, G., Wu, L., Liu, H., Lu, M., Fan, M., Wei, J., Chen, L., and Zheng, J.: Near-
- 897 real-time estimation of hourly open biomass burning emissions in China using multiple satellite retrievals,
- 898 Sci. Total Environ., 817, 152777, https://doi.org/10.1016/j.scitotenv.2021.152777, 2022.
- 899 Xu, Y., Huang, Z., Ye, J., and Zheng, J.: Hourly emissions of air pollutants and greenhouse gases from
- 900 open biomass burning in China during 2016-2020, Sci. Data, 10, 629, https://doi.org/10.1038/s41597-
- 901 023-02541-0, 2023a.
- 902 Xu, Y., Huang, Z., Ye, J., and Zheng, J.: Hourly emissions of air pollutants and greenhouse gases from
- open biomass burning in China during 2016–2020, Scientific data, 10, 629, 2023b.
- 904 Yin, S.: Biomass burning spatiotemporal variations over South and Southeast Asia, Environment
- 905 International, 145, 106153, https://doi.org/10.1016/j.envint.2020.106153, 2020.
- 906 Yu, Y., Mao, J., Wullschleger, S. D., Chen, A., Shi, X., Wang, Y., Hoffman, F. M., Zhang, Y., and Pierce,
- 907 E.: Machine learning-based observation-constrained projections reveal elevated global socioeconomic
- 908 risks from wildfire, Nat. Commun., 13, 1250, https://doi.org/10.1038/s41467-022-28853-0, 2022.
- 909 Zhang, F., Wang, J., Ichoku, C., Hyer, E. J., Yang, Z., Ge, C., Su, S., Zhang, X., Kondragunta, S., Kaiser,

https://doi.org/10.5194/essd-2025-515 Preprint. Discussion started: 21 October 2025 © Author(s) 2025. CC BY 4.0 License.



(a)

910	J. W., Wiedinmyer, C., and Da Silva, A.: Sensitivity of mesoscale modeling of smoke direct radiative
911	effect to the emission inventory: a case study in northern sub-Saharan African region, Environ. Res. Lett.,
912	9, 075002, https://doi.org/10.1088/1748-9326/9/7/075002, 2014.
913	Zhang, X., Kondragunta, S., Ram, J., Schmidt, C., and Huang, H.: Near-real-time global biomass burning
914	emissions product from geostationary satellite constellation, J. Geophys. Res.: Atmos., 117,
915	2012JD017459, https://doi.org/10.1029/2012JD017459, 2012.
916	Zhu, L., Val Martin, M., Gatti, L. V., Kahn, R., Hecobian, A., and Fischer, E. V.: Development and
917	implementation of a new biomass burning emissions injection height scheme (BBEIH v1.0) for the
918	GEOS-chem model (v9-01-01), Geosci. Model Dev., 11, 4103-4116, https://doi.org/10.5194/gmd-11-
919	4103-2018, 2018.
920	
921	
922	
923	
924	
925	
926	





Table 1. Statistics on the duration of sustained burning and periods of high probability of burning
 in different regions and vegetation types (Figure 1).

Regions	Vegetation	T_gap (hours) ^a	Filling periods (UTC)
1	Croplands	3	1-3
1	Forests	4	2-5
1	Grasslands	3	1-3
1	Peatlands	3	4-6, 20-22
1	Shrublands	10	1-10
2	Croplands	7	7-13
2	Forests	3	5-7
2	Grasslands	7	5-11
2	Peatlands	3	21-23
2	Shrublands	3	5-7
3	Croplands	3	6-8
3	Forests	10	0-9
3	Grasslands	3	1-3
3	Peatlands	3	20-22
3	Shrublands	9	0-8
4	Croplands	5	7-11
4	Forests	6	5-10
4	Grasslands	14	0-13
4	Peatlands	10	13-22
4	Shrublands	3	3-5

aT_gap: longest continuous fire duration within a high-burning period (frequency ≥ 0.9), allowing merging if separated by short gaps (mean frequency ≥ 0.5).





931 Table 2. Emission factors (unit: g kg⁻¹)

Species	Forest	Shrubland, Grassland	Cropland	Peatland
CO ₂	1570	1660	1430	1590
СО	113	69	76	260
NO_x	3.0	2.5	2.4	1.2
NH ₃	0.98	0.89	0.99	4.2
SO_2	0.70	0.47	0.80	4.3
PM _{2.5}	18.5	6.7	8.2	18.9
OC	10.9	3.0	4.9	14.2
BC	0.55	0.53	0.42	0.10



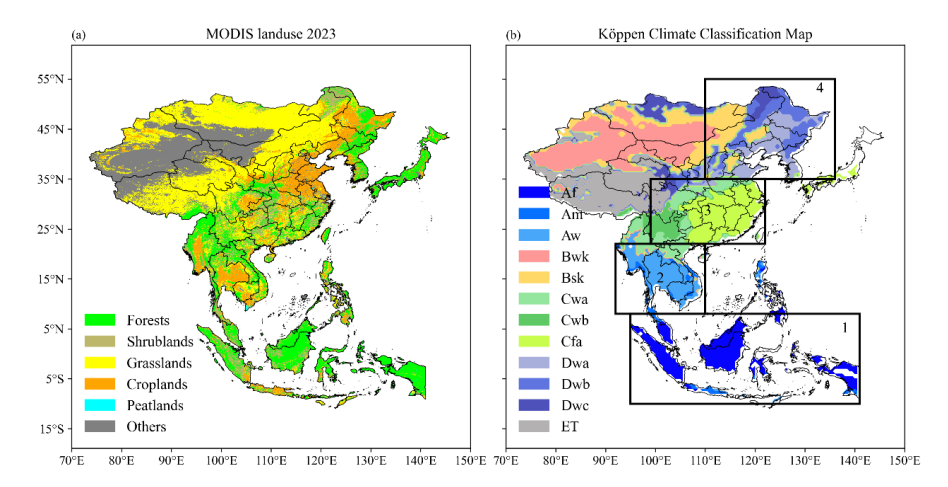


Figure 1. (a) MODIS land cover for 2023 in Southeast and East Asia. (b) Köppen climate classification Map (climate baseline 1991-2020), with representative high biomass burning emission regions based on Giglio et al., (2006), including 1. Southern Southeast Asia, 2. Mainland Southeast Asia, 3. Southern China, and 4. Northern China. Climate types include Af (tropical rainforest), Am (tropical monsoon), Aw (tropical savanna), Bwk (cold desert), Bsk (cold semi-arid), Cwa (humid subtropical with dry winter and hot summer), Cwb (temperate highland tropical climate with dry winter and warm summer), Cfa (humid subtropical with hot summer and no dry season), Dwa (humid continental with dry winter and hot summer), Dwb (humid continental with dry winter and cold summer), and ET (tundra).

958

959





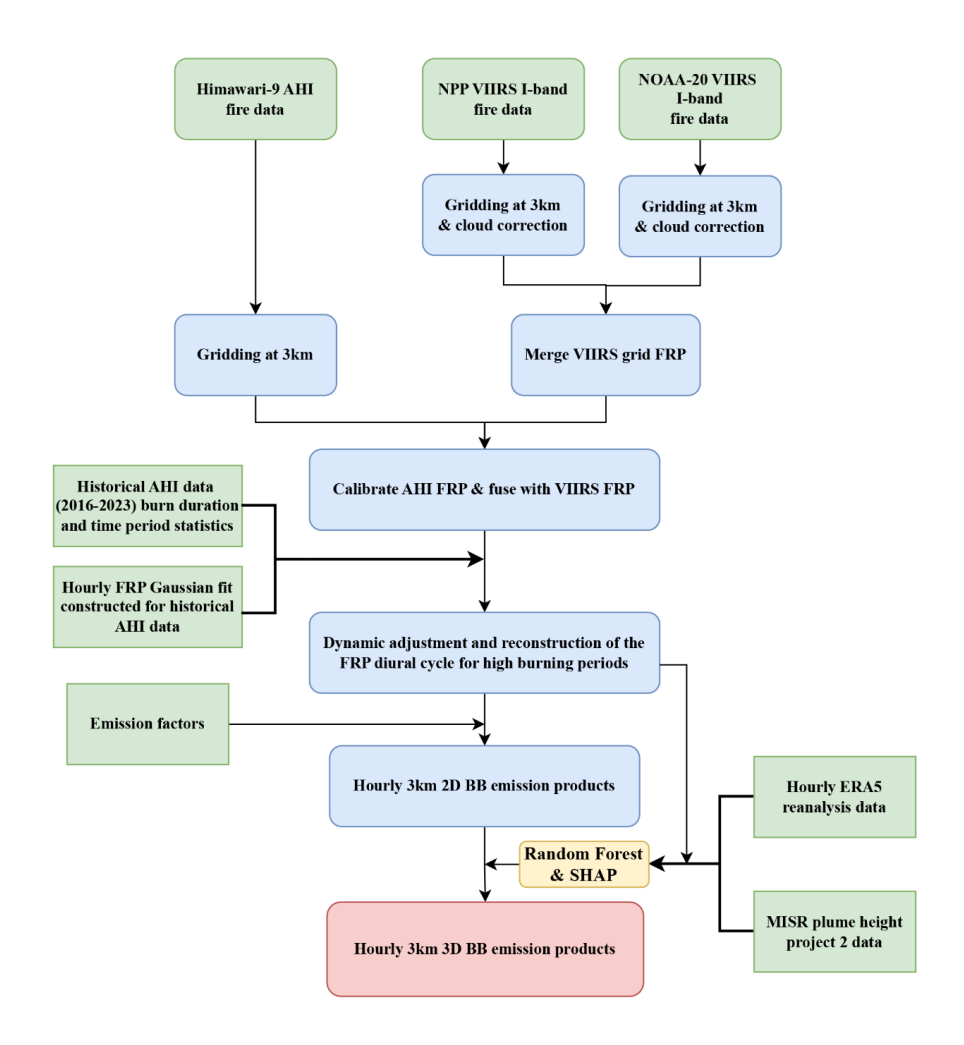


Figure 2. Methodological framework for constructing hourly three-dimensional biomass burning emission inventories in Southeast and East Asia.



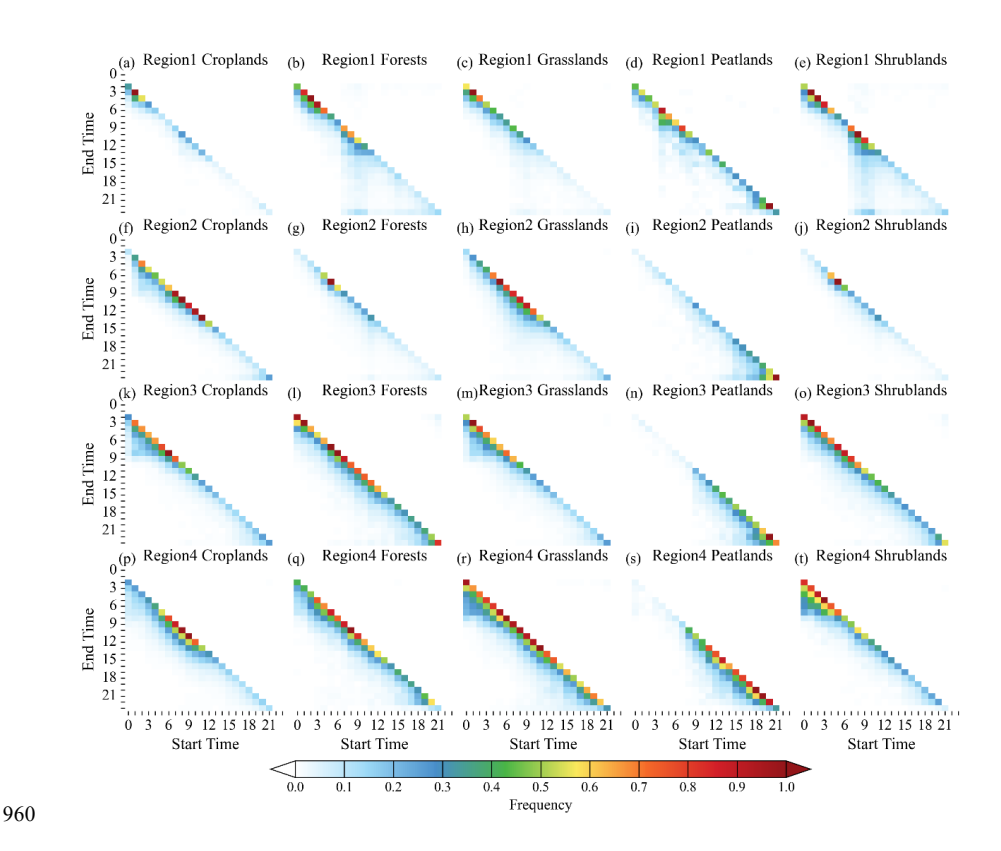


Figure 3. Characterizes the temporal distribution of sustained burning ≥ 3 hours in different regions and land types.



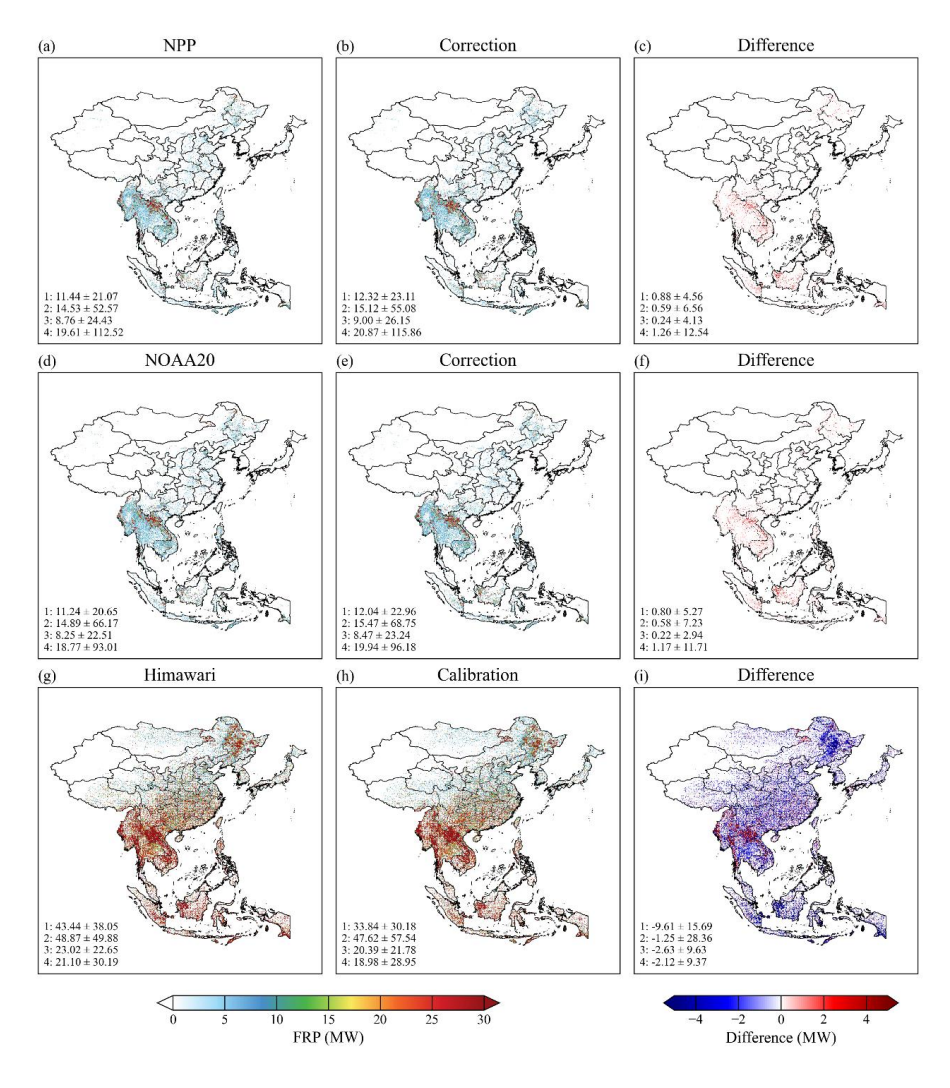


Figure 4. Cloud correction of gridded FRP data from VIIRS and AHI. The first row shows the correction for NPP, the second row for NOAA20, and the third row for Himawari-9. The last column displays the difference between the corrected and uncorrected FRP data.



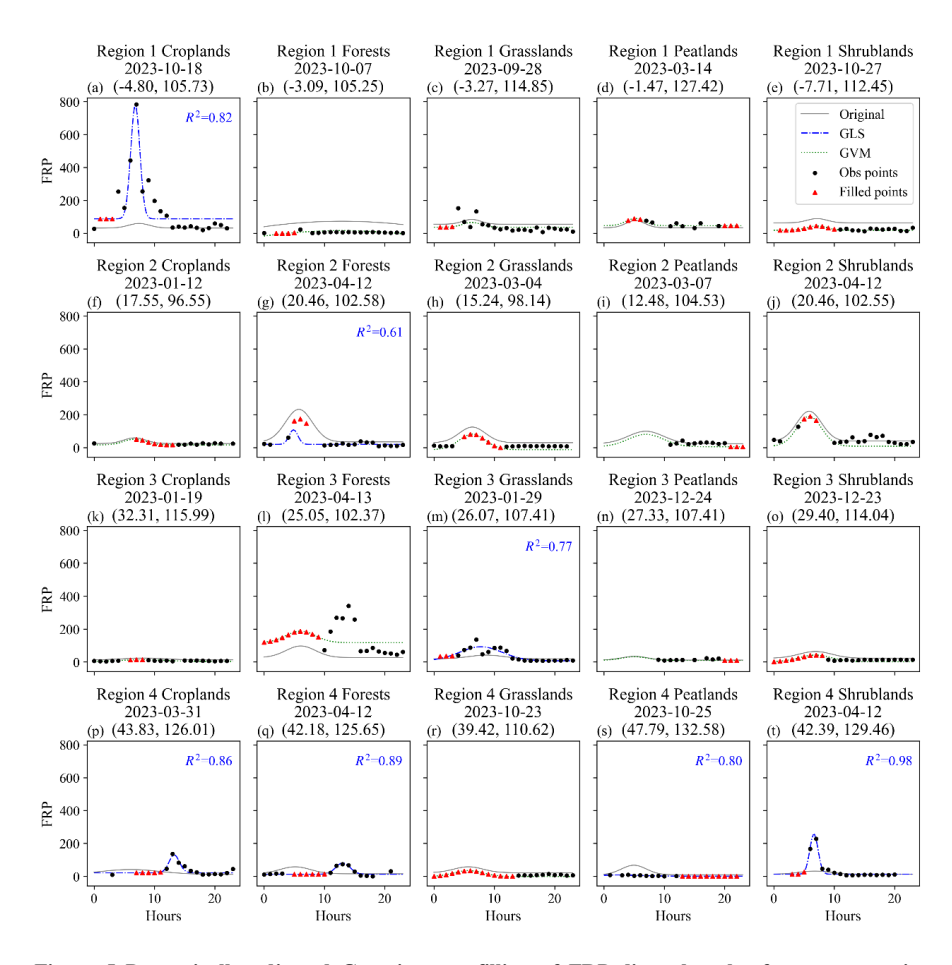


Figure 5 Dynamically adjusted Gaussian gap-filling of FRP diurnal cycles for representative regions and vegetation types in 2023. Solid black circles represent original observed FRP data, solid red triangles represent gap-filled FRP values for missing observations, gray solid lines are original climatological Gaussian fitting, blue dash-dot lines show dynamically adjusted Gaussian fitting results (Gaussian Least Squares, GLS), green dotted lines represent climatological Gaussian fitting with adjustment factor *d* only (Gaussian Vertical Movement, GVM).



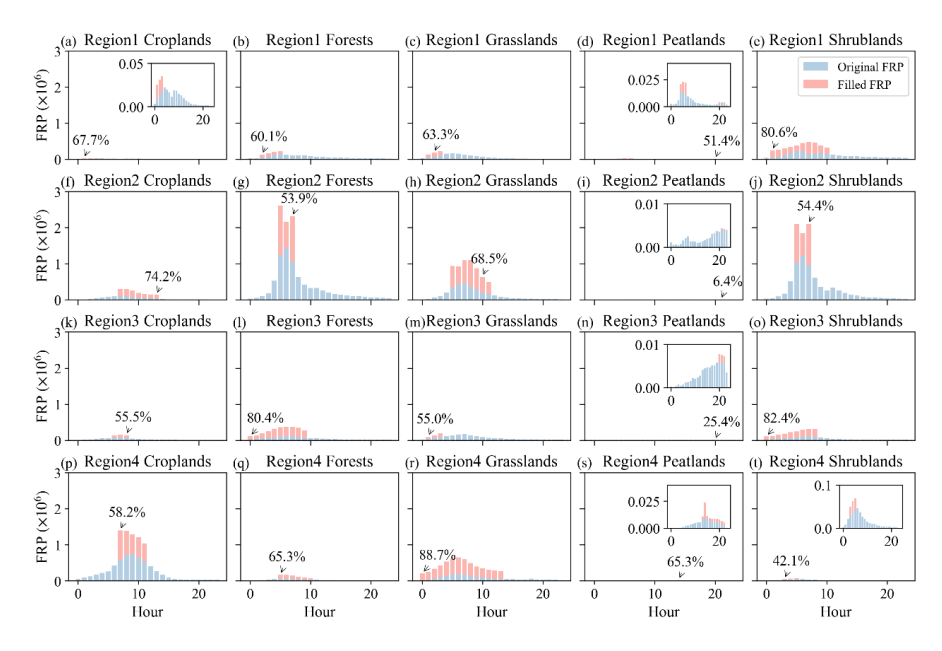


Figure 6. Bar chart comparing the total hourly FRP (2023) before and after Gaussian fitting adjustments across four climatic regions and five vegetation types. The time of the maximum proportion of filled FRP to unfilled FRP is also annotated, with some panels displaying enlarged insets.



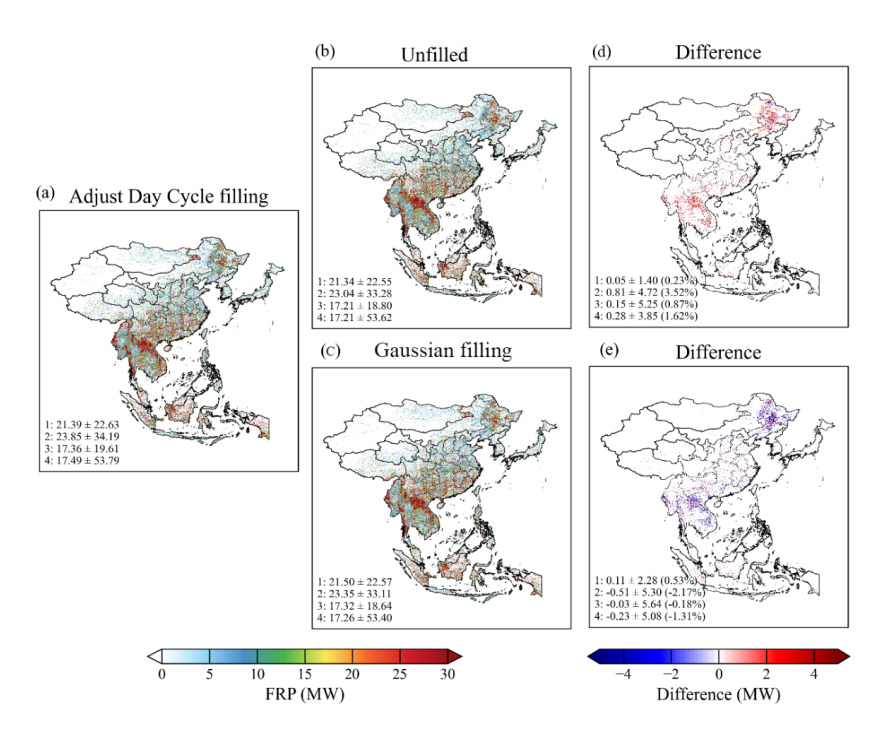


Figure 7 Spatial comparison of mean daily fire radiative power (FRP) distributions in the SEA region during 2023. (a) gap-filled dynamic reconstruction, (b) original observations, (c) traditional Gaussian fitting, (d) difference between (a) and (b), and (e) difference between (a) and (c).





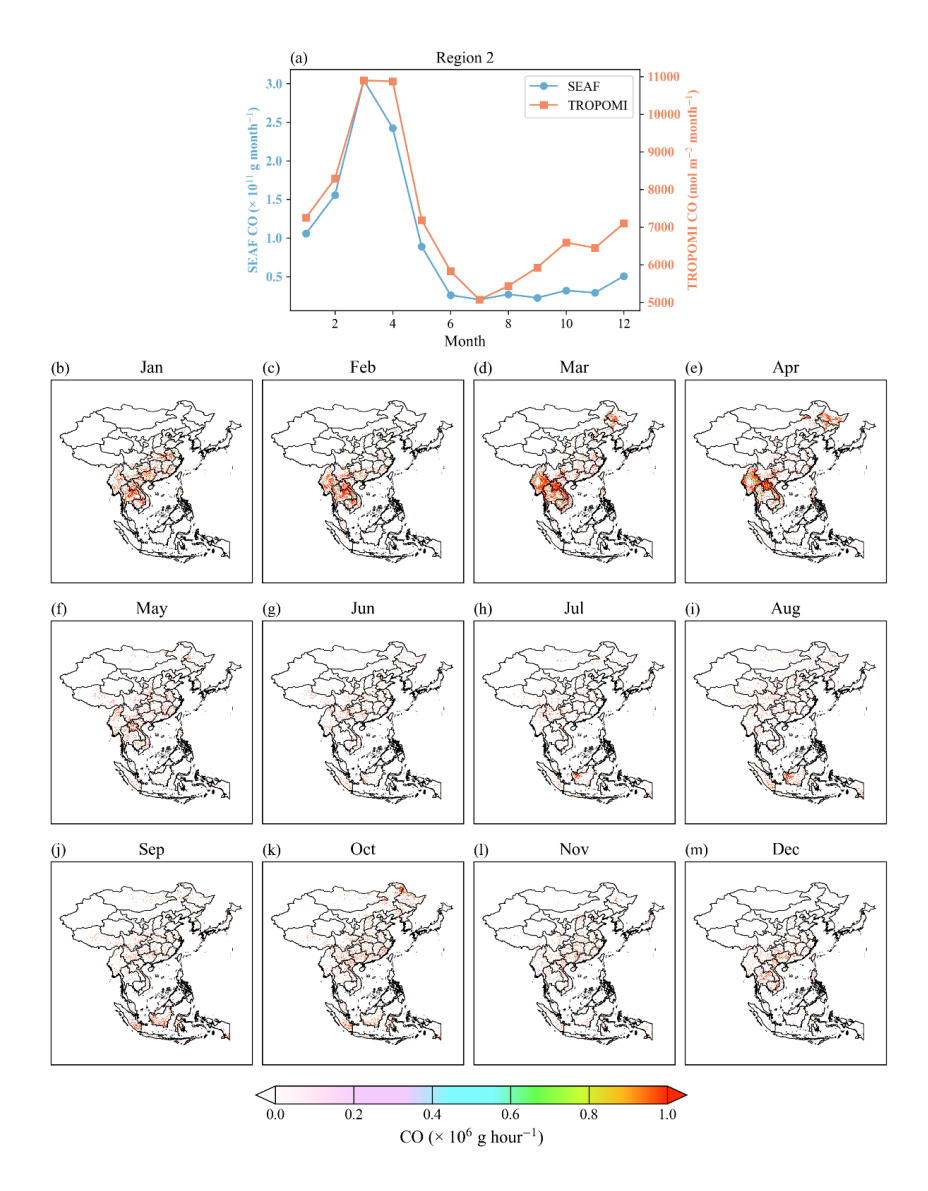


Figure 8 Monthly CO emissions over SEA in 2023 based on the SEAF inventory and comparison with satellite observations. (a) Temporal variation of monthly CO emissions from SEAF and CO column concentrations from TROPOMI over Region 2; (b-m) Spatial distribution of monthly mean CO emissions derived from SEAF.



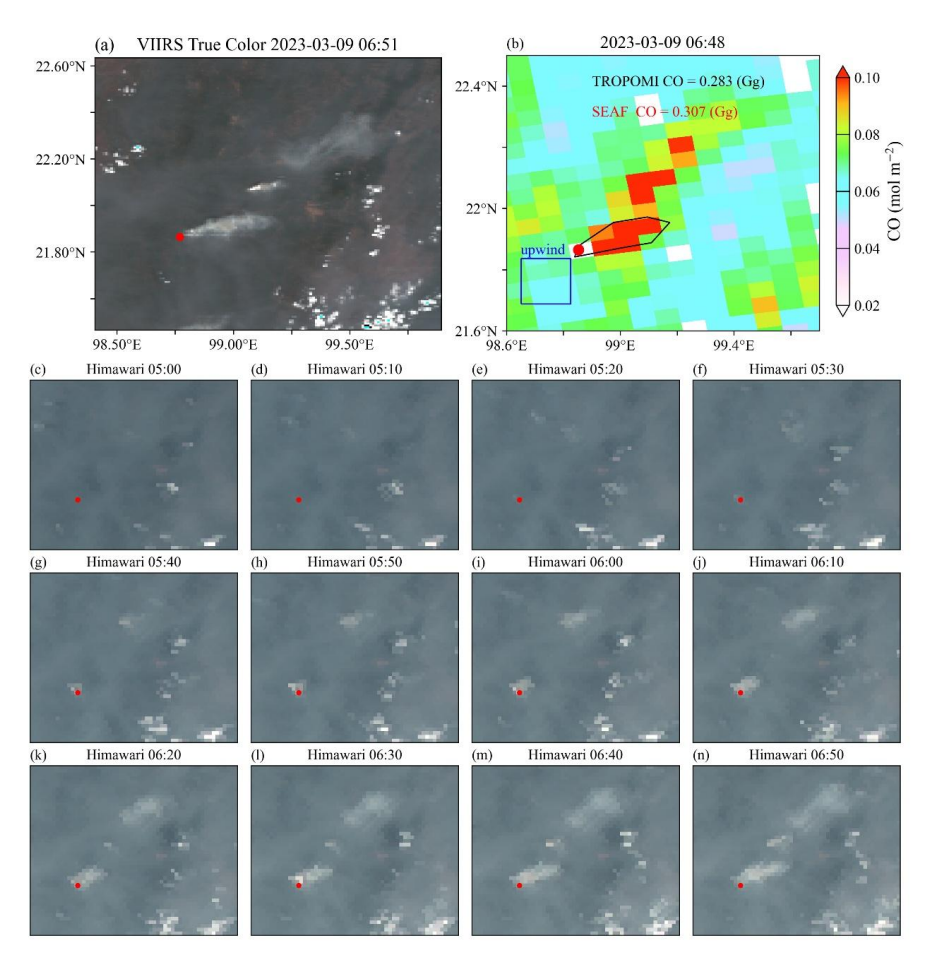


Figure 9 (a) True-color image from VIIRS, (b) comparison between CO emissions from TROPOMI observations and the SEAF emission inventory, and (c) true-color image from Himawari-9, with red dots indicating fire locations.

1017

1018

1019

1020





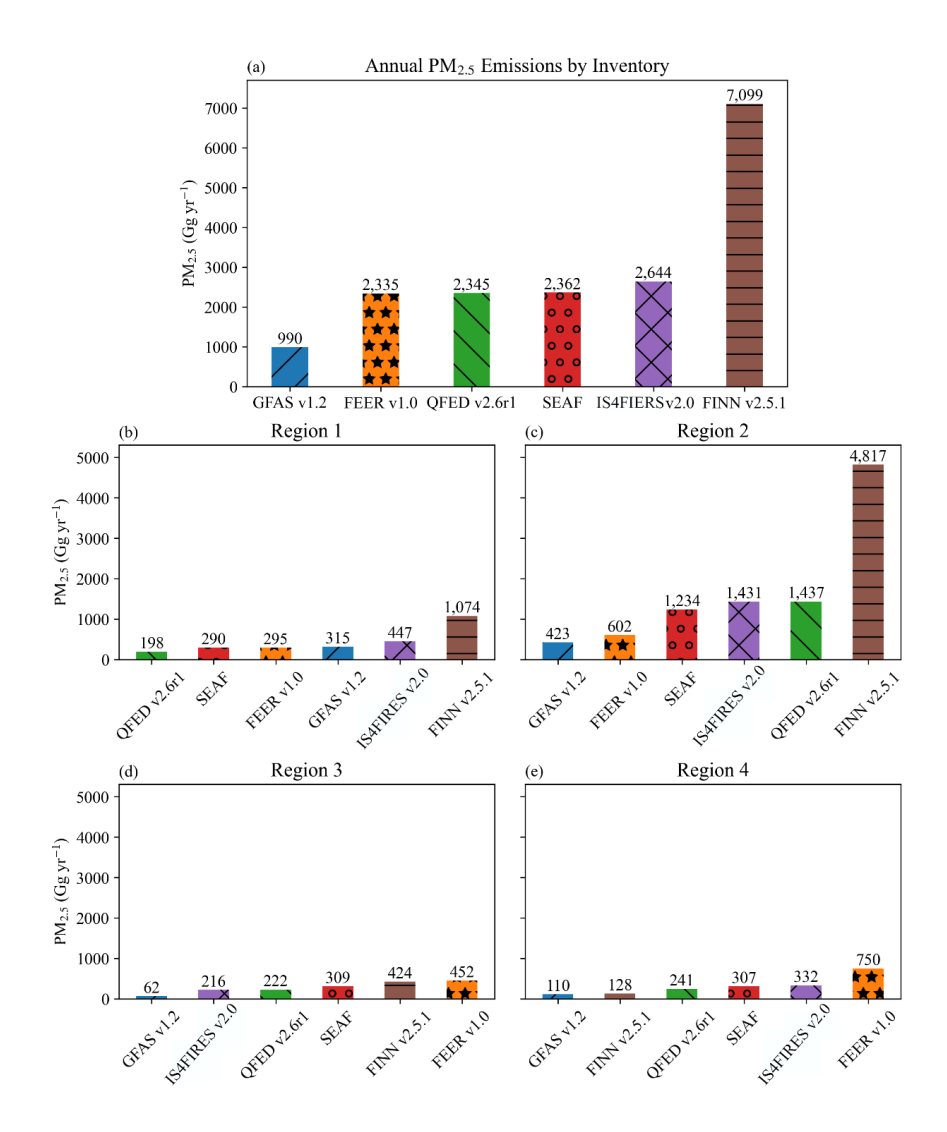


Figure 10 Comparison of SEAF PM_{2.5} emissions with five BB emission inventories.





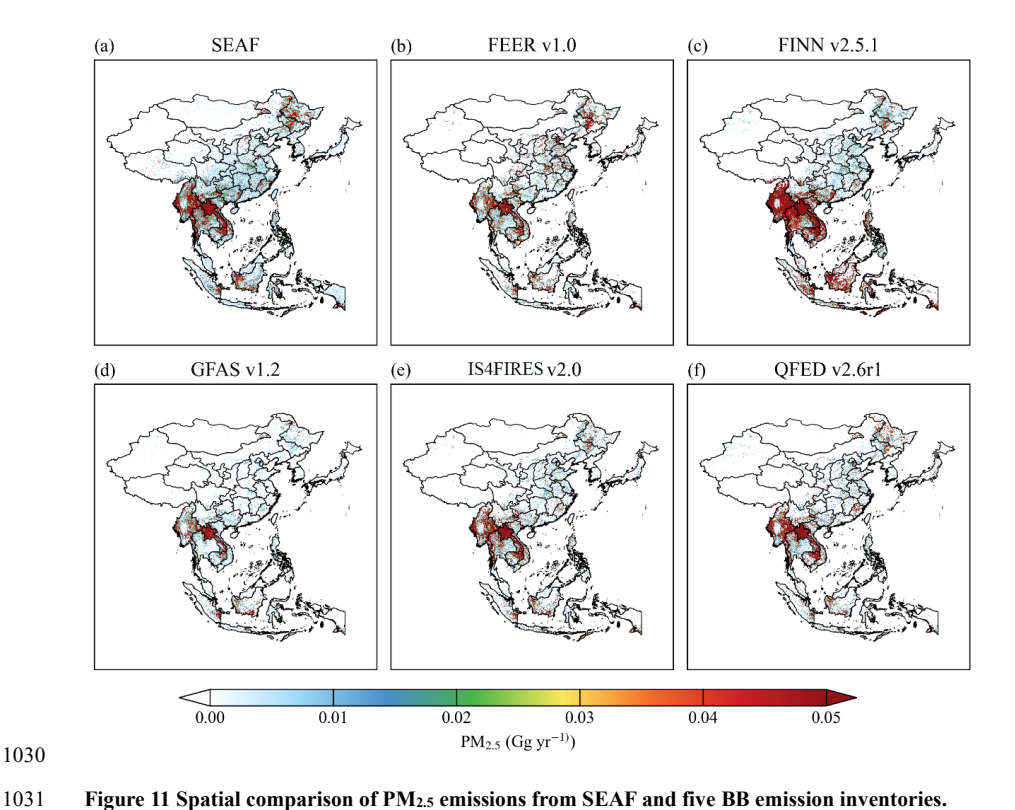


Figure 11 Spatial comparison of $PM_{2.5}$ emissions from SEAF and five BB emission inventories.

1034 1035





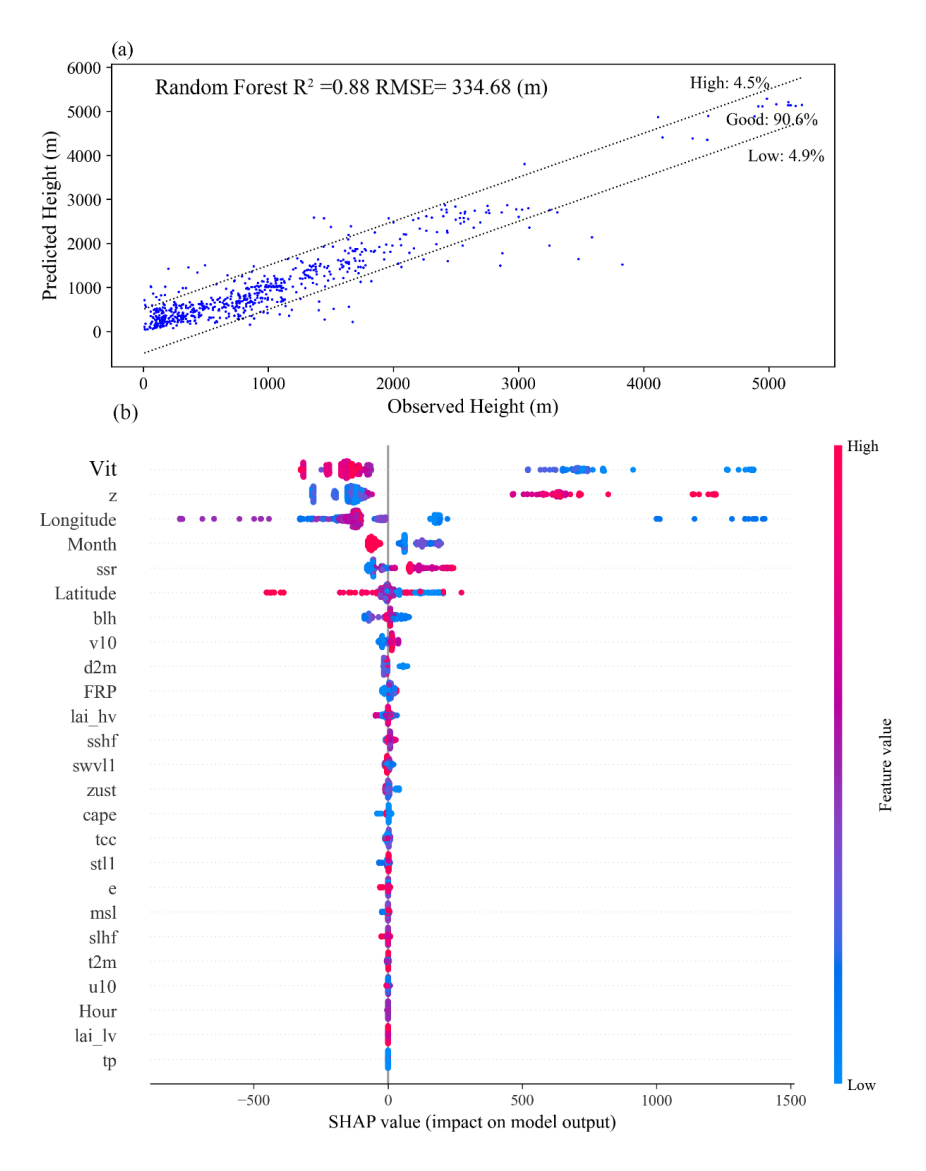


Figure 12 (a) Random Forest (RF)-based prediction of BB plume height and (b) SHAP-based analysis of key driving variables (Table S1).





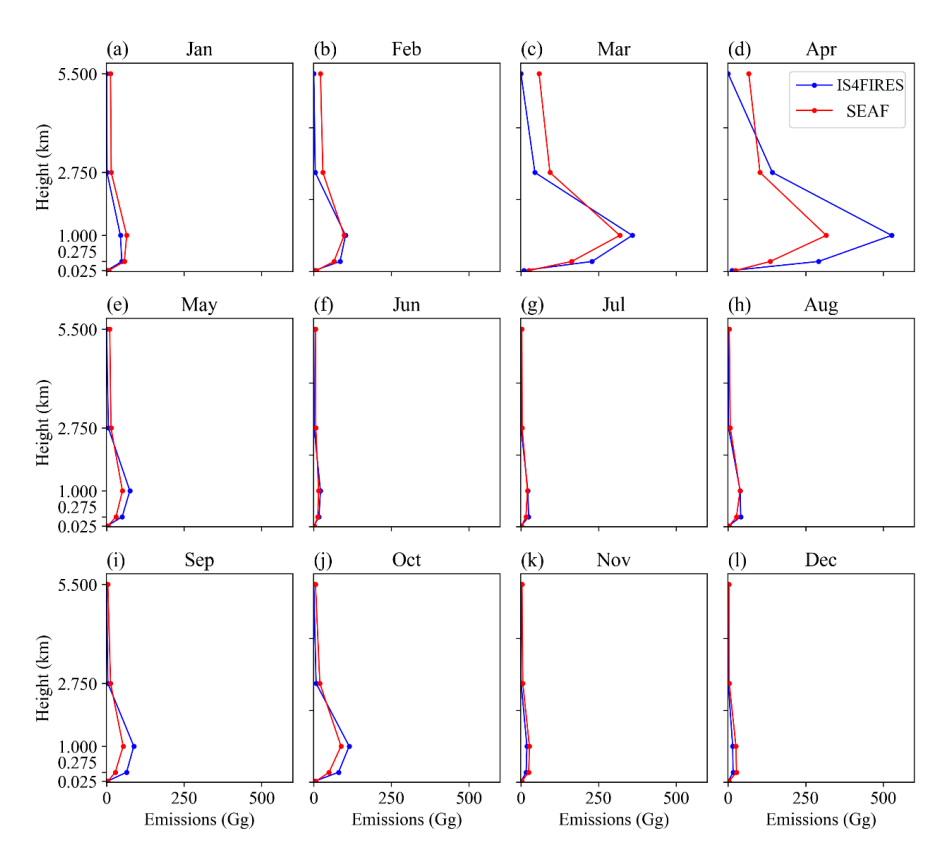


Figure 13 Vertical distribution comparison of SEAF and IS4FIRES PM_{2.5} (Jan-Dec) emissions.





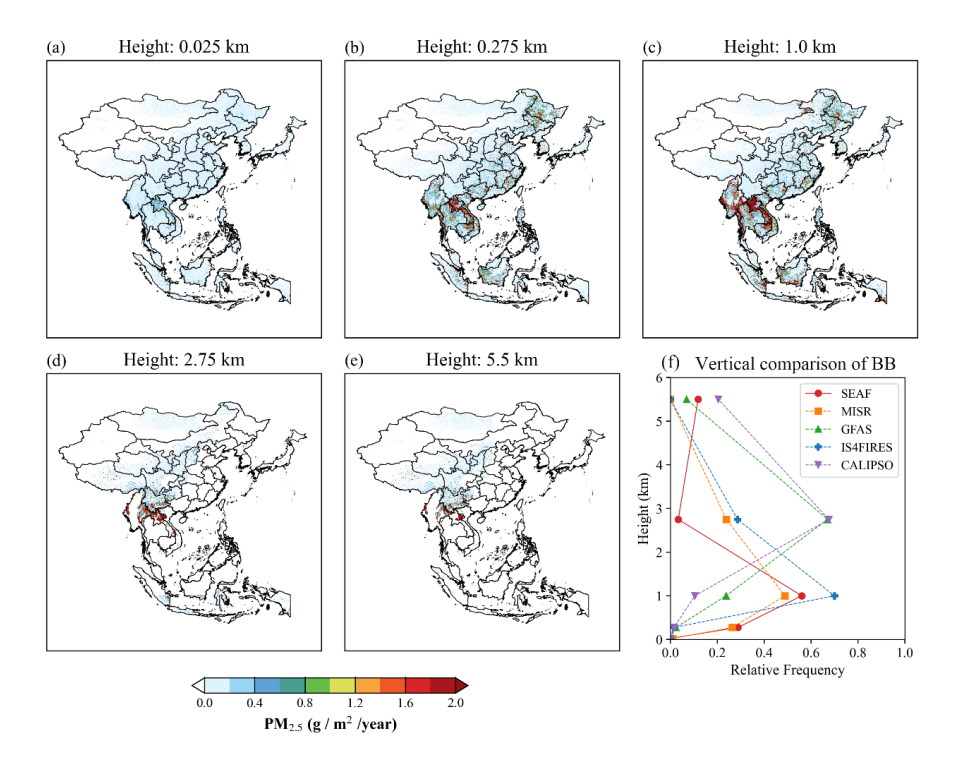


Figure 14 (a-e) Spatial distribution of SEAF $PM_{2.5}$ emissions at vertical five altitude levels (0.025-5.5 km), and (f) vertical comparison.

1049 1050